Advances in SQUID-detected magnetic resonance force microscopy

Wit, M. de

A

Feedback cooling of the cantilever's fundamental mode

The fundamental sensitivity of MRFM is limited by the thermal force noise. This noise can be reduced by lowering the temperature of the cantilever. However, this is complicated by the limited thermal conductance of all the different components combined with the constant influx of power from various sources. This can create large temperature gradients between the experiment's vital components, such as the sample and the cantilever, and the source of cooling (e.g. the mixing chamber). To give an example from Poggio et al.: in a cryostat with a base temperature of 250 mK, the cantilever temperature saturated at 2.2 K due to the laser used for the detection of the cantilever [44].

In this appendix, we discuss our efforts to cool the cantilever, focusing on the achieved cantilever temperature and thermal force noise, and the feedback cooling of our resonator to an effective mode temperature below 150 μK. Note that the experiments in this chapter were performed in one of the older versions of the setup than that explained in Ch. 2. All relevant experimental details will be discussed.

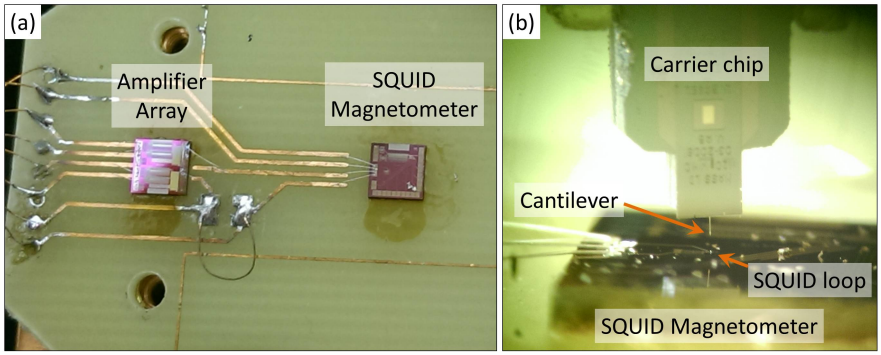

Figure A.1: Setup used for the experiments described in this section. (a) Photograph of the improvised two-stage SQUID, consisting of a magnetometer coupled to a SQUID array. (b) Optical microscope image of the cantilever placed directly above the SQUID loop of the magnetometer.

A.1 Cantilever temperature and thermal noise force

In order to achieve the lowest possible cantilever temperature, several measures were taken to ensure a good thermalization to the mixing chamber of the dilution refrigerator. First of all, the silicon chip which supports the cantilever is attached to a copper block using a brass spring, and further thermalized using some silver epoxy at the base of the chip. This copper block is directly connected to the mixing chamber via a silver wire with a diameter of 1 mm and a length of about 30 cm. When we assume the silver is the limiting factor in the thermal conductance, this configuration leads to an optimal power tolerance of 3 nW/mK at 100 mK. However, since this estimate ignores the thermal resistance at the interfaces of different components and materials, the actual thermal conductance should be much lower.

To determine the lowest temperature at which the cantilever saturates, we place the cantilever directly above a SQUID[1] (see Fig. A.1) in order to maximize the coupling and thereby the SNR. We measure the thermal motion of the cantilever by looking at the power spectral density of the SQUID signal at different temperatures. Two representative curves measured at 12 mK and 500 mK can be seen in the upper image of Fig. A.2. The thermal motion of the cantilever's fundamental mode at 2727 Hz is clearly visible above the noise. We use a cantilever with a magnet with a radius of 1.5 µm, and a stiffness of 50 µN/m. The smaller bumps visible in the bottom

[1]PTB GX1GFM Magnetometer, connected to a PTB 5X1GF4 SQUID series Array used as amplifier

curve are mechanical vibrations of the setup amplified by the transfer function of the cantilever.

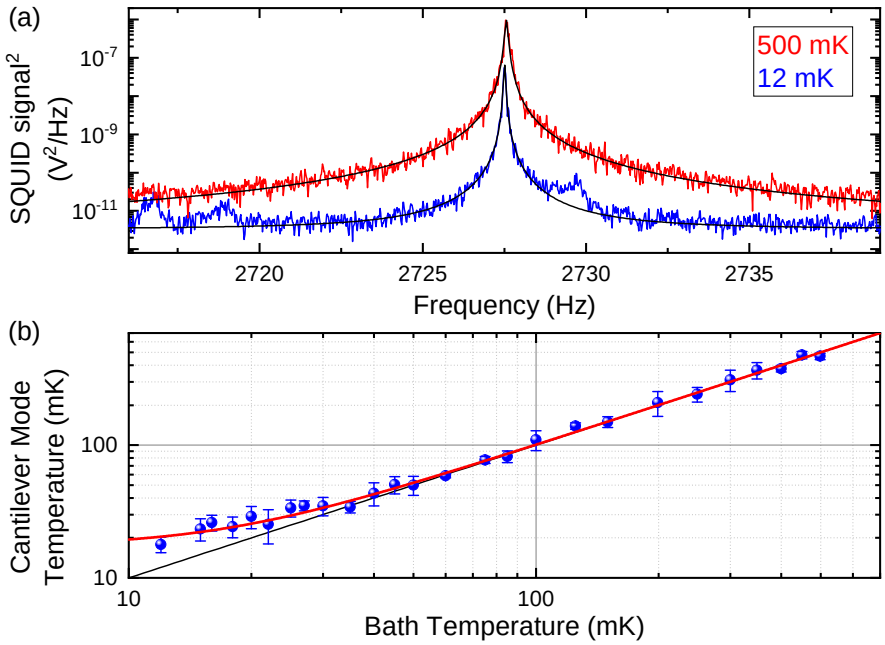

Figure A.2: (a) SQUID signal for two bath temperatures. The black lines are Lorentzian fits to the data. (b) Cantilever noise temperature calculated from the area beneath the peaks obtained from the fit. The red solid line is a fit to the data using Eq. A.2, with $T_0 = 17.3 \pm 3.3$ mK, and $n = 2.2 \pm 0.6$.

Once the coupling between the magnetic particle and the SQUID is known, the area obtained from a fit of the data to a Lorentzian peak can be used to calculate the effective mode temperature, and via the equipartition theorem [2] this can be translated to the mean square displacement of the resonator. The coupling, which depends on the position of the cantilever with respect to the SQUID, can be experimentally determined by using a calibration coil in the SQUID input coil circuit to drive the cantilever [53]. Alternatively, the coupling can be determined by assuming that at high temperatures the cantilever temperature is equal to the bath temperature. This gives us

$$\frac{1}{2}k\langle x\rangle^2 = \frac{1}{2}k_{\mathrm{B}}T = \frac{1}{2}k_{\mathrm{B}}\ \beta A \tag{A.1}$$

[2] The equipartition theorem relates the thermal energy of a system to its average potential energy. In the case of an harmonic oscillator, it simply states that $\frac{1}{2}k_{\mathrm{B}}T = \frac{1}{2}k\langle x\rangle^2$.

with β the conversion factor between the area and the temperature in units K/V^2, and A the area under the curve of the power spectral density.

The measured cantilever noise temperature is shown in Fig. A.2(b). Our assumption that at high temperatures the cantilever temperature is equal to the bath temperature is justified by the linear behavior observed above approximately 50 mK, as indicated by the black diagonal line. Below this temperature, a saturation of the cantilever noise temperature can be observed. The red solid line is a fit to the data using a saturation curve [47]:

$$T_{\mathrm{N}} = (T^{\mathrm{n}} + T_0^{\mathrm{n}})^{1/\mathrm{n}} \tag{A.2}$$

The best fit to the data was obtained when using a saturation temperature $T_0 = 17.3 \pm 3.3$ mK, and an exponent $\mathrm{n} = 2.2 \pm 0.6$, where the value of the exponent n is determined by the temperature dependence of the limiting thermal resistance. The acquired value for n indicates that the thermal conductance is due to conduction electrons [109], whereas the first Oosterkamp MRFM setup, which was used in the work of Usenko et al. [47], appeared to be limited by phonon processes or boundary effects. This difference could be due to the improved direct electrical connection of the cantilever to the mixing chamber via the silver wire and silver epoxy. Since the thermal conductance via electrons is much better than via phonons at low temperatures, this might also explain the reduction in the saturation temperature of the cantilever by nearly a factor of 2 when compared to the work by Usenko et al..

By using the conversion factor defined in Eq. A.1, we can now use the SQUID signal power spectral density to calculate the displacement noise, as shown in Fig. A.3.

With the data we have gathered so far, we can calculate some numbers which indicate the final measurement sensitivity of our setup, such as the thermal force noise, which is given by

$$\sqrt{S_{\mathrm{F}}} = \sqrt{4k_{\mathrm{B}}T\frac{k}{2\pi f_0 Q}} \tag{A.3}$$

In recent years, several groups have reached astonishingly low values for the thermal force noise, reaching well within the zeptoNewton range, using a variety of resonator geometries [228–231]. However, most of these geometries are unsuited for MRFM. For our cantilever, assuming $k = 50$ μN/m, $f_0 = 2727$ Hz and $Q = 5{\cdot}10^4$ at low temperatures, we calculate a force noise $\sqrt{S_{\mathrm{F}}} = 0.23$ aN/$\sqrt{\mathrm{Hz}}$. This value is very close to the lowest values ever reported for the soft cantilever geometries necessary for magnetic resonance force microscopy [45, 232, 233].

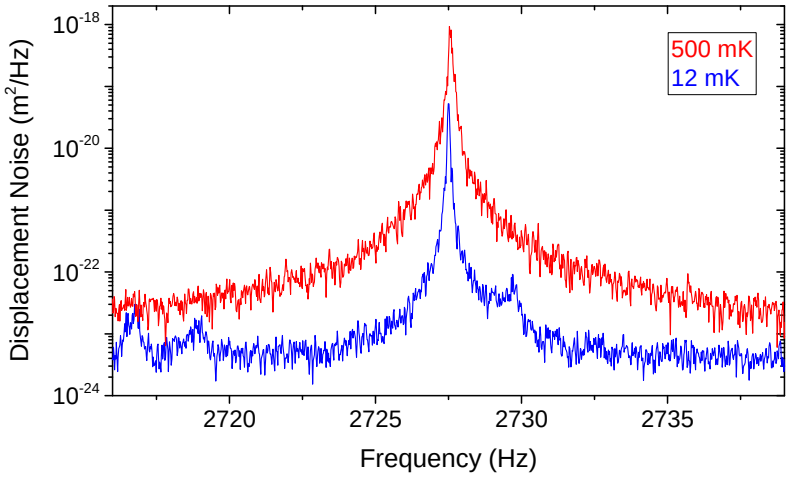

Figure A.3: Displacement spectra showing the thermal motion of the cantilever for temperatures of 500 mK (red) and 12 mK (blue).

A.2 Feedback cooling of the cantilever's fundamental mode

Since the effective temperature of our resonator appears to be limited by the performance of the dilution refrigerator, the next step to reduce the motion of the resonator is to implement a technique called feedback cooling. In this technique, a high precision measurement of the motion of a resonator is used to perform active feedback on said motion, thus introducing an additional damping of the resonator. Feedback cooling is widely used for a variety of reasons:

- One of the ultimate goals is to use MRFM to detect the magnetic moments of individual nuclei with Ångström-scale spatial resolution. Detecting such small forces requires the smallest possible spring constant. However, since the mean-square amplitude of a cantilever's Brownian motion is given by $\langle x^2 \rangle = k_\mathrm{B}T/k$, reducing the spring constant might lead to a thermal motion exceeding the desired imaging resolution [234]. Furthermore, the Brownian motion of the resonator also introduces a fluctuation of the polarizing field felt by the spins with an amplitude of $B_x = x_\mathrm{rms}\partial B/\partial x$ [235]. To solve these issues feedback cooling must be used to reduce the cantilever's motion to within an acceptable range.

- As the quality factor of a resonator increases, its bandwidth is reduced. Since

the amplitude of a resonator decays with a typical time $\tau = Q/\pi f_0$, the time between independent measurements becomes very large. By reducing the quality factor using feedback, the decay time can be kept short, which increases the bandwidth of the experiment without sacrificing the force sensitivity [57].

- A cold resonator with a low number of phonons is useful for a variety of experiments exploring the limits of quantum mechanics [236–238]. This topic is extensively covered in the thesis of de Voogd [59].

The setup used for the feedback cooling experiment was the same as the one used in the previous section on the effective cantilever temperature, but at a position with a slightly better coupling to the pickup loop, which affects the detection noise floor.

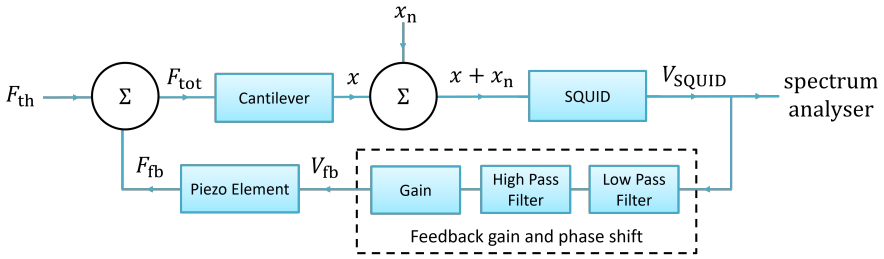

Figure A.4: Diagram of the experimental setup used for the feedback cooling

In order to perform the feedback, the SQUID signal containing the information about the cantilever motion is sent through a low-pass filter followed by a high-pass filter[3] to add a gain and phase shift. The bandwidth of both filters is adjusted to obtain the desired phase shift with a random attenuation. This signal is then sent to an amplifier with a tunable gain[4]. This altered signal is then sent to a piezoelectric element which is mechanically coupled to the cantilever. A diagram of this setup can be seen in Fig. A.4. When the phase shift is set in such a way that the feedback is negative, this scheme results in a damping of the cantilever motion, proportional to the velocity of the cantilever. Simultaneously, the SQUID signal is sent to a spectrum analyzer to measure the resulting cantilever motion.

The response of the cantilever to this feedback signal can be calculated from an equation of motion very similar to the one defined in Eq. 2.10, but with an additional force term [44]:

$$m\ddot{x} + \Gamma\dot{x} + kx = F_{tot} = F_{th} - g\gamma\left(\dot{x} + \dot{x}_n\right), \tag{A.4}$$

[3]SRS SIM965 Analog Filter
[4]SRS SIM911 BJT Preamp

where F_{th} is the random thermal force, g the gain of the feedback, and x_{n} is the detector displacement noise. The reason this last term is present here and not in Eq. 2.10, is that now also the detector displacement noise is coupled back to the cantilever motion via the feedback mechanism.

Considering this equation of motion, the spectral density of both the actual displacement and the measured displacement of the cantilever can be calculated, following Poggio et al. [44]. The actual displacement spectral density is given by

$$\begin{aligned} S_{\mathrm{x}}(\omega) = &\left[\frac{1/m^2}{\left(\omega_0^2-\omega^2\right)^2+\left(1+g\right)^2\frac{\omega_0^2\omega^2}{Q_0^2}}\right] S_{\mathrm{F}} \\ &+\left[\frac{g^2\omega_0^2\omega^2/Q_0^2}{\left(\omega_0^2-\omega^2\right)^2+\left(1+g\right)^2\frac{\omega_0^2\omega^2}{Q_0^2}}\right] S_{\mathrm{x_n}}, \end{aligned} \tag{A.5}$$

and the measured displacement spectral density by

$$\begin{aligned} S_{\mathrm{x+x_n}}(\omega) = &\left[\frac{1/m^2}{\left(\omega_0^2-\omega^2\right)^2+\left(1+g\right)^2\frac{\omega_0^2\omega^2}{Q_0^2}}\right] S_{\mathrm{F}} \\ &+\left[\frac{\left[\left(\omega_0^2-\omega^2\right)^2+\omega_0^2\omega^2\right]/Q_0^2}{\left(\omega_0^2-\omega^2\right)^2+\left(1+g\right)^2\frac{\omega_0^2\omega^2}{Q_0^2}}\right] S_{\mathrm{x_n}}, \end{aligned} \tag{A.6}$$

with $S_{\mathrm{x_n}}$ the spectral density of the detection noise, and $S_{\mathrm{F}} = 4k_{\mathrm{B}}T\Gamma$ the standard thermal force spectral density with T the cantilever temperature at zero gain.

The result of the feedback cooling of the cantilever, starting from a Q-factor of $5.2 \cdot 10^4$ at a temperature close to 20 mK is shown in Fig. A.5. The solid lines are fits to the data according to Eq. A.6. Fitting the data can be challenging due to the high number of parameters and, especially in the case of the purple curve, the low SNR. In the procedure we followed, we fix the parameters for the mass and spring constant by calculating them based on the cantilever geometry. For T, we take the calibrated cantilever temperature based on the procedure described in section A.2. We fix Q_0 at the value obtained from a Lorentzian fit to the data at zero gain. This only leaves three parameters free: the resonance frequency f_0, the gain g, and the detection noise $S_{\mathrm{x_n}}$.

This procedure works well for all but the highest gain data. To get a reliable value for the gain for this data, we also fix f_0 and $S_{\mathrm{x_n}}$ to the values found for the second highest gain. The gain we obtain in this way can then be used to calculate

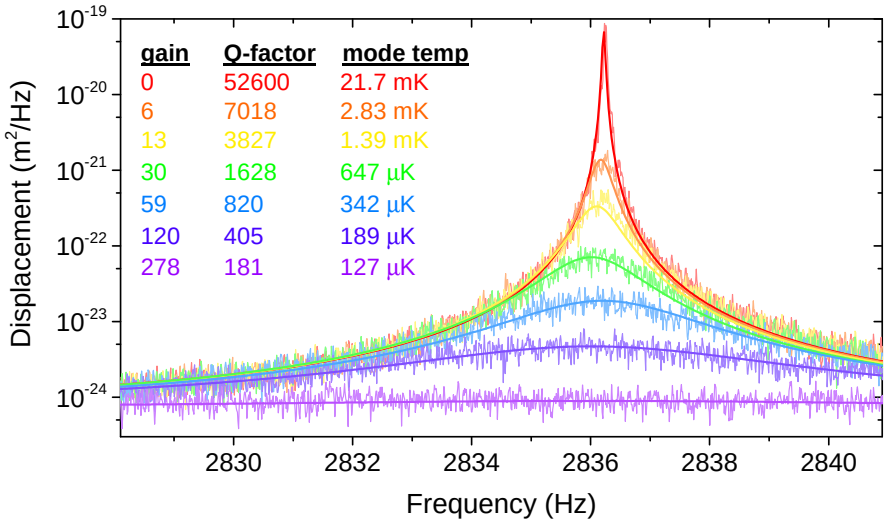

Figure A.5: The main result of the feedback cooling, indicating a final mode temperature of 127 µK. The solid curves are fits to equation A.6. The Q factors of all curves (apart from the bottom one) are obtained from a Lorentzian fit to the data.

the Q using $Q = Q_0/(1+g)$ [48, 239].

The fit values obtained from Fig. A.5 can be used to calculate the final mode temperature achieved by the feedback cooling, using [44]

$$T_{\mathrm{mode}} = \frac{T}{1+g} + \frac{k\omega_0}{4k_{\mathrm{B}}Q_0}\left(\frac{g^2}{1+g}\right)S_{\mathrm{x_n}}, \tag{A.7}$$

from which we find that at our maximum gain (limited by the detection noise) we have achieved a mode temperature of 127 µK. The minimal achievable temperature is given by

$$T_{\mathrm{min}} = \sqrt{\frac{k\omega_0 T}{k_{\mathrm{B}}Q_0}S_{\mathrm{x_n}}} = 122\ \mu\mathrm{K}, \tag{A.8}$$

given our parameters and measured force noise.

This mode temperature corresponds to a phonon occupation number

$$N_{\mathrm{phonons}} = \frac{k_{\mathrm{B}}T_{\mathrm{mode}}}{\hbar\omega_0} = 937, \tag{A.9}$$

at a thermal force noise of 0.23 $\mathrm{aN}/\sqrt{\mathrm{Hz}}$ and a displacement noise floor of 840 $\mathrm{fm}/\sqrt{\mathrm{Hz}}$.

B

Limitations of the mechanical generation of radio-frequency fields

While the higher modes have the potential for generating very large B_1 fields with very little dissipation, we have also encountered some serious drawbacks of the presence and use of the higher modes. In this appendix, we will demonstrate some of these limitations based on saturation experiments performed on copper, as described in Ch. 4.

B.1 Off-resonant coupling

The first issue we discuss is the unintended driving of one or more of the higher modes, even when the applied RF pulse is far off-resonance with the higher mode. During the pulse, the cantilever higher mode acts like a forced damped harmonic oscillator, with equation of motion

$$\ddot{x}(t) + \Gamma\dot{x}(t) + \omega_0^2 x(t) = \frac{F_0}{m} cos(\omega t), \tag{B.1}$$

with m the mass of the oscillator, $\omega_0^2 = k/m$ the natural frequency, Γ the damping, and F_0 the amplitude of the external force. For $\omega \neq \omega_0$, no damping, and the initial conditions where the cantilever is stationary at t = 0, the general solution is given by

$$x(t) = 2A_0 \sin\left[\frac{(\omega_0 + \omega)t}{2}\right] \sin\left[\frac{(\omega_0 - \omega)t}{2}\right], \tag{B.2}$$

with

$$A_0 = \frac{F_0/m}{\omega_0^2 - \omega^2}. \tag{B.3}$$

So, if $\omega \approx \omega_0$, we can look at $x(t)$ as the product of a slow modulation with an amplitude $2A_0 \sin((\omega_0 - \omega)t/2)$, and a rapid oscillation with amplitude $\sin((\omega_0 + \omega)t/2)$. The amplitude of the modulation increases as ω approaches ω_0. When $\Gamma > 0$, the motion decays to zero as time progresses, resulting in a steady oscillation with amplitude

$$A(\omega) = F_0 / \left[m^2(\omega_0^2 - \omega^2)^2 + \Gamma^2\omega^2\right]^{(-1/2)} \tag{B.4}$$

When the pulse is switched off, the cantilever motion starts to decay following

$$x(t) = A_1 \exp(-\omega_0 t/2Q) \cos(\omega_0 t), \tag{B.5}$$

where A_1 is the amplitude of the cantilever at the end of the pulse. We assume weak damping.

We demonstrate the effect of this behaviour in Fig. B.1(a), where we show the direct frequency shift after an RF pulse with a frequency of 950 kHz, which is in between the higher modes at 756 kHz and 1009 kHz, and very short pulse durations. We observe an oscillation of the direct frequency shift, which in the past was wrongfully interpreted as a potential Rabi oscillation [205]. The period of the oscillation is 18 µs, which indicates that it originates for the beating with the higher mode at 1.009

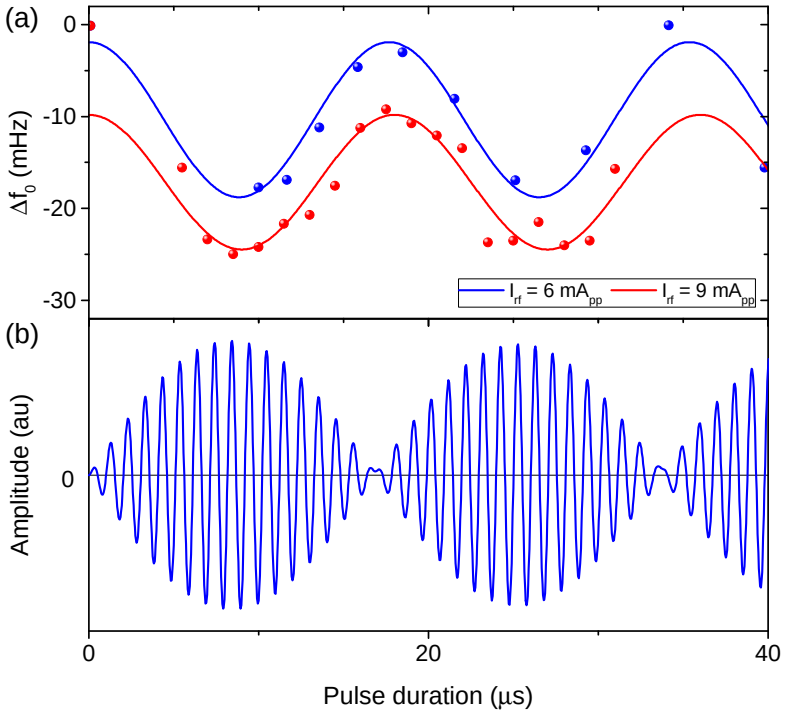

Figure B.1: (a) Direct frequency shift Δf_0 versus pulse duration at RF frequency f_{RF} = 950 kHz, T = 30 mK, and h = 0.95 μm, for 2 different B_1 fields. The solid curves are fits to a simple cosine, from which we extract oscillation periods of 17.7 ± 0.3 and 18.0 ± 0.2 μs for the 6 and 9 mA_{pp} data sets, respectively. (b) Simulation of the motion $x(t)$ of the 1.009 MHz higher mode when excited by a 950 kHz drive force.

MHz, 59 kHz off-resonance. Fig. B.1(b) shows the simulated amplitude of the 1.009 MHz higher mode when excited with a periodic driving force at 950 kHz.

Thus, the "Rabi" oscillations observed for very short pulse times are in reality caused by the motion of one or more of the higher modes, generating a B_{RF} field with an amplitude which varies with the slow beating frequency, and with a duration determined by the exponential decay with characteristic time $\tau = Q/\pi f_n$.

B.2 Non-linearities

The second issue is the inherent non-linearity of the higher modes of the cantilever. In Fig. B.2(a) we vary the frequency of the drive field we use to excite the higher mode at 756 kHz. We drive the higher mode using RF currents of about 3 μA_{pp} (black), 10 μA_{pp} (red), and 30 μA_{pp} (green). The solid lines in the figure are guides to the eye. The asymmetry of the curves shows that even at extremely small driving amplitudes the non-linearities of the cantilever dominate the total B_{RF} field.

In Fig. B.2(b) we see a measurement where we drive the same higher mode, but now far away from the sample. In this case, we drive the mode using the cantilever piezo, and we measure the response using the induced magnetic field in the pickup loop. Also far from the surface we observe a clear non-linearity, indicating that at least parts of the non-linearity are an inherent property of the cantilever. We assume that the non-linearities are caused by stress at the surface of the cantilever, which would mean this issue intensifies for higher mode numbers. The slight mismatch between the mode frequency in both figures is attributed to a small sample-induced frequency shift in the top figure.

B.3 Temperature dependence of quality factor

Finally, we report a large temperature-dependence of the quality factor of the higher modes on the cantilever temperature. Measurements of the temperature-dependence of the Q-factor for the 756 kHz mode is shown in Fig. B.3(b). The solid red line in this curve indicates a $1/T$ dependence. The precise origin of the dissipation responsible for this Q-factor is unknown. For low temperatures, the Q-factor increases to over $5{\cdot}10^5$, with a characteristic time $\tau > 0.2$ s. For higher frequency modes, Q-factors in excess of 1 million have been observed.

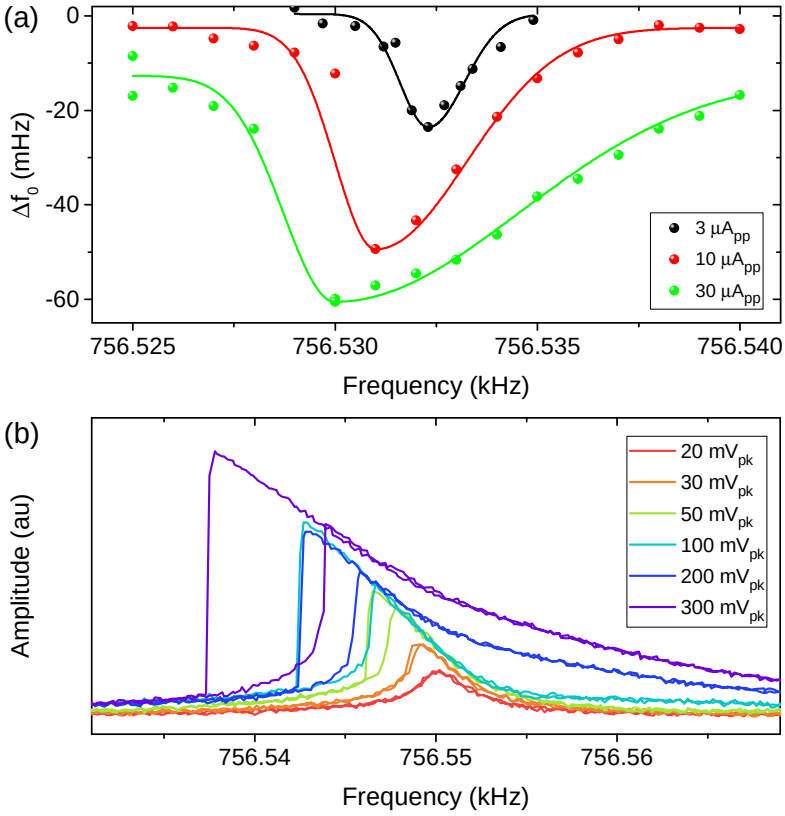

Figure B.2: (a) Direct frequency shift Δf_0 for various drive frequencies around the higher mode frequency. The amplitude of the RF currents are 3 μA_{pp} (black), 10 μA_{pp} (red), en 30 μA_{pp} (green). The solid lines are guides to the eye. An asymmetry of the signal and thus B_{RF} field generated by the higher mode indicates a strong non-linearity of the mode. (b) Response of the higher mode when driven by the cantilever piezo at various drive amplitudes far away from the sample. The drive frequency is swept from frequencies below the resonance to frequencies above the resonance and back. The signal is obtained from the magnetic field measured by the SQUID.

It is possible to convert the Q-factor to a dissipation constant. The shape of the higher vibrational modes of the cantilever induces a rotation of the magnet at the tip of the cantilever, which means we can calculate the dissipation constant using

$$\Gamma_n = \frac{\kappa_n}{Q\omega_n}, \tag{B.6}$$

where κ_n is the torsional spring constant, given by

$$\kappa_n = \omega_n^2 I, \tag{B.7}$$

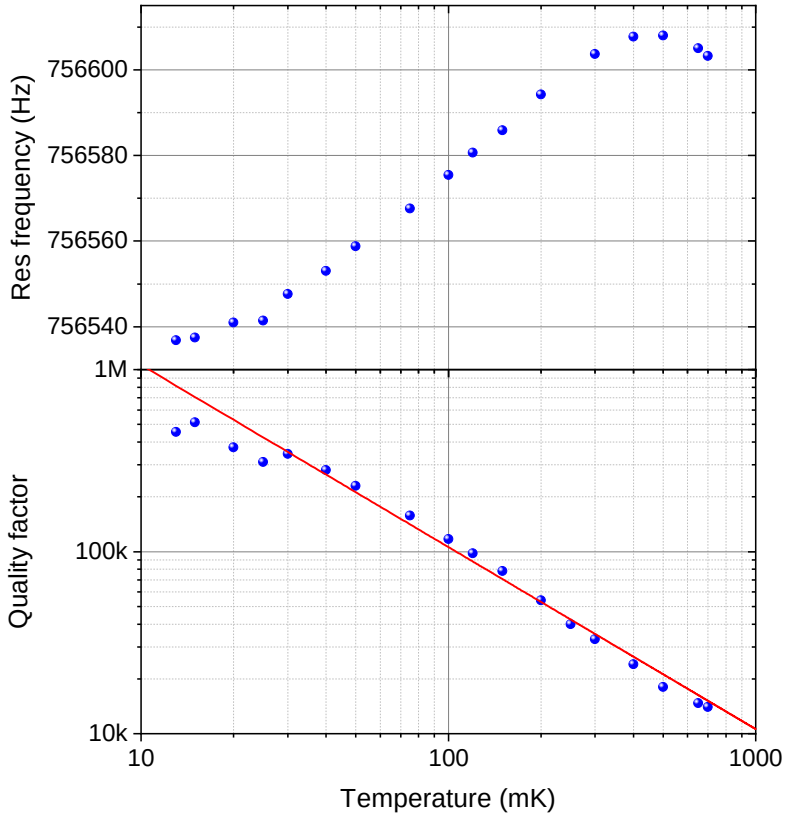

Figure B.3: (a) Resonance Frequency and (b) quality factor of the higher mode at 756 kHz measured for different temperatures of mass 3, when the magnetic particle is far away (> 5 µm) from the surface. The red solid line in (b) indicates a 1/T dependence.

with I the moment of inertia. When we assume the moment of inertia is dominated by the rotation of the heavy spherical magnet, it is given by $I = (2/5)mR_0^2$ with $m = 2 \cdot 10^{-13}$ kg the mass of the magnet and with $R_0 = 1.7$ µm the radius. If we take the 6^{th} higher mode at 756 kHz as an example, we find $\kappa_6 = 5 \cdot 10^{-12}$ Nm/rad, which at a temperature of 20 mK leads to a dissipation constant $\Gamma_6 = 3 \cdot 10^{-24}$ kg m^2/s and a thermal torsional noise of about 2 yNm/$\sqrt{\text{Hz}}$. However, our detection sensitivity is not sufficient to detect the thermal motion for most of the higher modes.

C

Quenching of SQUID modulation under radio-frequency interference

In this appendix, we briefly expand upon the results presented in Ch. 6, in particular Fig. 6.5, to show the influence of the amplitude of the RF interference or crosstalk on the depth of the SQUID modulation, and the corresponding SQUID noise.

C.1 Quenched SQUID modulation

As we have seen in Ch. 6, the peak-to-peak amplitude of the SQUID modulation (ΔV_m) is reduced when the SQUID is exposed to a large RF flux. When we apply a test flux Φ_a to the SQUID in combination with RF interference Φ_{rf}, the time-dependent SQUID voltage response to Φ_a is given by [152]:

$$V(t) = \Delta V_{\mathrm{m}} \cdot \cos \frac{2\pi\Phi_{\mathrm{a}}}{\Phi_0} \cdot J_0 \left(\frac{2\pi\Phi_{\mathrm{rf}}}{\Phi_0} \right), \tag{C.1}$$

with $\Phi_0 = 2.068 \cdot 10^{-15}$ Wb the magnetic flux quantum, and J_0 the zeroth-order Bessel function. In Ch. 6 we only looked at the response of the SQUID voltage under a constant RF amplitude, but we can also reconstruct the entire response by varying the RF amplitude. The result of this measurement can be seen in Fig. C.1 for a constant frequency RF interference at 1908 kHz. We applied a text flux using the generator of the SQUID electronics with an amplitude of a little over $2\Phi_0$. The inset shows an example of the SQUID modulation for this applied test flux combined with RF flux at constant amplitude and constant frequency.

Since we have only measured the absolute amplitude, the data follows the absolute value of the zeroth-order Bessel function, shown as the red solid line. For a peak RF flux of $0.38\Phi_0$ the amplitude of the SQUID modulation is reduced to zero,

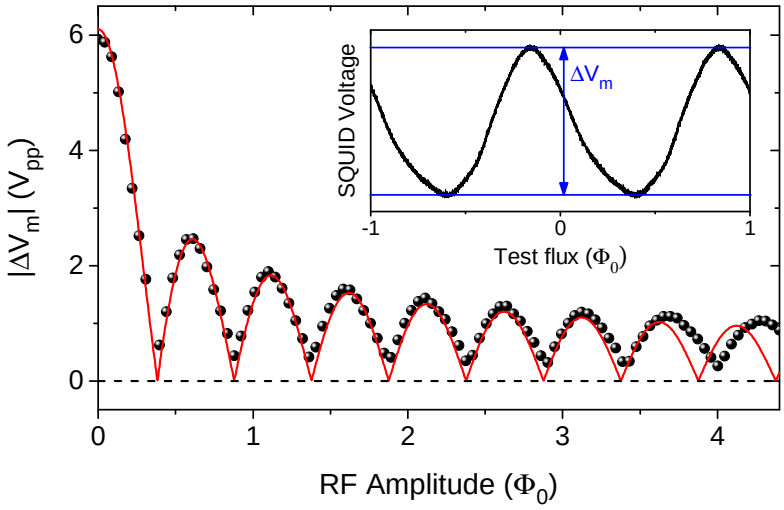

Figure C.1: Measured SQUID modulation depth as a function of the amplitude of the RF interference. This inset shows the way the modulation depth is extracted from the raw SQUID-flux response. The red solid line is a fit to Eq. C.1.

independent of the test flux Φ_a. For large RF amplitude we see that the period of the oscillation increases. An increasing period means that the amplitude of the RF interference reaching the SQUID reduces. We speculate that this is linked to the observed dissipation of power for high frequency, high amplitude RF fields, as described in Ch. 7. The idea behind this hypothesis is that we can make the data and fit match by stretching the horizontal axis by a value proportional to the RF amplitude squared. This scaling is consistent with the amplitude-dependent heating observed. An experimental check for this hypothesis would be to repeat the experiment at a higher RF frequency, as the dissipation of the RF wire scales as $f^{1.5}$ for high f. In that case, the deviation of the data from the fit should appear at lower RF amplitudes. This check has not been done yet.

C.2 Possibilities

The measurement presented in Fig. C.1 might have important consequences for SQUID-based MRFM experiments, if for some reason the compensation scheme presented in Ch. 6 cannot be used. For example in experiments on electrons, where the required GHz-range frequencies pose a challenge for the compensation. In those cases, the negative effects that the pulse has on the SQUID modulation can be reduced by selecting a suitable amplitude for the pulse.

Furthermore, one could use a measurement such as that presented in Fig. C.1 to check the amplitude of the magnetic field that we create at the location of the sample because the geometry of the pickup loop is known. Especially in the case of GHz pulses this cannot be done directly using the SQUID because of the limited bandwidth, but the amplitude of the pulse might show up in the amplitude of the SQUID modulation.

D

Fabrication recipes

This appendix discusses some of the basic fabrication recipes used for the work presented in this thesis, as we believe this might be useful for future students.

D.1 Detection chip

We start the fabrication of the MRFM detection chips from 350 nm thick NbTiN films grown on top of a silicon wafer. All details about this film are given by Thoen et al. (our films are grown using the Nordiko 2000 Static) [55]. The pickup loop and RF wire are fabricated with a top-down approach using reactive-ion-etching (RIE). We use the following fabrication recipe:

Resist and spincoating:

- Resist: Negative E-beam resist AR-N 7700.18.
- Spincoat at 1500 rpm for a thickness of 0.65 μm.
- Bake at 80°C for 90 seconds on a closed hotplate.

Exposure using Raith EBPG 5000+ at the Kavli Nanolab Delft:

- E-beam dose 150 $\mu C/cm^2$.
- Spotsize 66 nm. With proximity effect correction (PEC).

Development after exposure:

- Postbake at 110°C for 120 seconds on a closed hotplate.
- MF321 developer, 180 seconds.
- H_2O, 30 seconds.
- Rinse with H_2O, dry with nitrogen.

Reactive-ion-etching using Leybold F2 at the Kavli Nanolab Delft:

- 13.5 sccm SF_6, 5.0 sccm O_2.
- 50 W forward RF power, 8 W backward RF power. 320 V_{DC} bias.
- Etching time: 335 seconds + 10 second overetch.
- O_2 plasma descum to help in resist removal.
- 20 sccm O_2, 30 W forward RF power, 100 seconds.

Stripping of the resist before dicing:

- PRS-3000 (positive-resist stripper), 40°C, sonicate for 15 minutes.
- Acetone, 40°C, sonicate for 5 minutes.
- IPA, 40°C, sonicate for 5 minutes.
- Rinse with IPA, dry with nitrogen.

Dicing of the detection chips at the Kavli Nanolab Delft:

- Apply positive photoresist S1805 to prevent surface damage during dicing.
- Spincoat at 4000 rpm.
- Bake at 110°C for 120 seconds on a closed hotplate.
- Dice using DAD 3220 wafer dicer.

Resist stripping after dicing:

- PRS-3000, heated to 85°C au bain-marie, 15 minutes.
- Move beaker to sonicator, sonicate for 5 minutes.
- Reheat to 85°C au bain-marie, 10 minutes.
- Move beaker to sonicator, sonicate for 5 minutes.
- Acetone, room temperature, sonicate for 5 minutes.
- IPA, room temperature, sonicate for 5 minutes.
- Rinse with IPA, dry with nitrogen.

Final measured thickness of the structures on the chip using DektakXT in Leiden: 400 nm, approximately 350 nm NbTiN and 50 nm overetch into the silicon substrate.

D.2 Double layer resists for sputtering

For sample fabrication using sputtering, a double resist layer with an undercut is required for proper lift-off and to prevent dog-ears. We identified 2 recipes which seem to work well with the available sputtering machines.

Recipe 1: thin samples.

Resist and spincoating:

- Spincoat PMMA 200k, AR-P 642.06, 4000 rpm. Thickness 0.2 μm.

- Bake at 180°C for 180 seconds on open hotplate.
- Spincoat PMMA 950k, AR-P 672.042, 4000 rpm. Thickness 0.25 µm.
- Bake at 180°C for 180 seconds on open hotplate.

Optimal E-beam dose: 280 µC/cm^2. Suitable for samples with a thickness of up to about 150 nm. Very large undercut due to large difference in polymer length.

Recipe 2: thick samples.

Resist and spincoating:

- Spincoat PMMA 600k, AR-P 662.06, 4000 rpm. Thickness 0.4 µm.
- Bake at 180°C for 180 seconds on open hotplate.
- Spincoat PMMA 950k, AR-P 672.042, 4000 rpm. Thickness 0.25 µm.
- Bake at 180°C for 180 seconds on open hotplate.

Optimal E-beam dose: 300 µC/cm^2. Suitable for samples with a thickness of up to about 350 nm, at the expense of a smaller undercut.

Development and lift-off.

Both options are developed following the same recipe:

- MIBK:IPA (1:3), 60 seconds.
- IPA (stopper), 30 seconds.
- Rinse with IPA, dry with nitrogen.

Liftoff after sample deposition:

- Acetone, 52°C, 20 minutes.
- Spray with acetone while keeping the chip submerged.
- Transfer to clean acetone, sonicate for 2 minutes.
- Inspection of the chip using an optical microscope, still submerged in acetone.
- When lift-off successful, sonicate in ethanol for 2 minutes.
- Sonicate in IPA for 2 minutes.
- Rinse with IPA, dry with nitrogen.

D.3 Specific samples

In this section, we will briefly discuss the recipes used for the specific samples used in the experiments presented in this thesis.

D.3.1 Copper

We aim for a sample consisting of about 100 nm of copper, capped with a 10-20 nm layer of gold to prevent oxidation. Deposition of both layers is done in a single session (without venting the system) using the Leybold Heraeus Z406 sputtering system in Leiden. Before sputtering, we do a 4-5 second long dip in hydrofluoric (HF) acid to remove oxides from the surface of the detection chip, followed by three H_2O baths. The chip is dried using nitrogen.

The chip is then loaded into the Z406 within minutes to prevent re-oxidation of the surface as much as possible. The chip is glued to the sample holder using silver paint to improve cooling. Sputtering is started from a background pressure of $5.5{\cdot}10^{-6}$ mbar. We use the following sputtering parameters:

- Cu layer: $5{\cdot}10^{-3}$ mbar argon, flow 49 sccm. RF voltage 1 kV. Pre-sputtering for 3 minutes, final sputtering for 10 minutes.
- Au layer: $5{\cdot}10^{-3}$ mbar argon, flow 49 sccm. RF voltage 1 kV. Pre-sputtering for 3 minutes, final sputtering for 90 seconds.

Measured thickness of the combined Cu/Au layer using DektakXT: 130 nm.

D.3.2 Calcium fluoride

We start from a sample ordered from Kurt J. Lesker, containing crystalline calcium fluoride pieces (1-4 mm) with a purity of 99.99%. The deposition was done using resistance evaporation, inspired by earlier work by Mamin et al. [14]. To improve thermalization, the CaF_2 is deposited on top of a thin layer of copper and gold. The copper and gold are deposited using e-beam evaporation in the Leybold Heraeus L560 at the Kavli Nanolab. The parameters for the different materials are:

- Cu layer: e-beam, 12 kV. Evaporation time 100 seconds at a rate of 0.8-1.2 Å/s.
- Au layer: e-beam, 12 kV. Evaporation time 375 seconds at a rate of 1.0-1.2 Å/s.
- CaF_2 layer: resistive heating, 25% power. Evaporation time 610 seconds at a rate of 3-5 Å/s.

Measured thickness of the Cu/Au layer using DektakXT: 40 nm. Measured thickness of the CaF_2 layer: 240 nm.

D.3.3 Palladium

Target ordered from ESPI: purity 99.99%, with less than 2 ppm Fe. The sputtering is done in the UHV sputtering system in Leiden. Before sputtering, we do a 4-5 second long dip in hydrofluoric (HF) acid to remove oxides from the surface of the detection chip, followed by three H_2O baths. The chip is dried using nitrogen. After the HF dip, the chip is loaded into the vacuum as soon as possible ($<$ 20 minutes).

Sputtering is started at a chamber pressure of $7.7{\cdot}10^{-9}$ mbar. Sputtering is done using an argon pressure of $3.3{\cdot}10^{-3}$ mbar. The RF power is set to 100 mA, 401V. We pre-sputter for 5 minutes to clean the target, then do real sputtering on the sample for 20 minutes. The measured thickness of the palladium layer using the DektakXT is 108 nm.

D.4 Considerations for double-layer detection chips

As discussed in Ch. 2, it is worth to invest time in the development of double-layer detection chips. This would enable the fabrication of on-chip transformers to boost the coupling efficiency between the pickup loop and SQUID input coil, and would also open the possibility to fabricate gradiometric pickup loops that cross the RF wire to reduce flux crosstalk. The first attempts to fabricate these double-layer devices were done by de Voogd [59]. In these attempts, the first layer was fabricated following a similar recipe as described in Sec. D.1 (RIE etching), while the second layer was made using a lift-off process. At the visual inspection after the sputtering of the second NbTiN layer, it was found that the resist was cracked. The measured critical current of the second layer, which was much lower than expected with only several

μA, confirms that the second layer was contaminated, probably from the resist which could not stand the high temperatures during sputtering.

From this we conclude that structures made by sputtering and lift-off might be more susceptible to contamination, resulting in a material with a lower critical current density. Hence, it is preferable to make the RF wire and the secondary coil of a transformer from the first (reactive-ion-etched) layer of high thickness NbTiN, as especially the RF wire should be able to carry large currents when used for an NMR experiment.

Bibliography

[1] Sidles, J. A. Noninductive detection of single-proton magnetic resonance. *Appl. Phys. Lett.*, 58(24):2854–2856, 1991.

[2] Burley, S. K., Berman, H. M., Bhikadiya, C., Bi, C., Chen, L., Di Costanzo, L., Christie, C., Dalenberg, K., Duarte, J. M., Dutta, S., et al. Rcsb protein data bank: biological macromolecular structures enabling research and education in fundamental biology, biomedicine, biotechnology and energy. *Nucleic Acids Res.*, 47(D1):D464–D474, 2018.

[3] Rugar, D., Yannoni, C. S., and Sidles, J. A. Mechanical detection of magnetic resonance. *Nature*, 360(6404):563, 1992.

[4] Züger, O. and Rugar, D. First images from a magnetic resonance force microscope. *Appl. Phys. Lett.*, 63(18):2496–2498, 1993.

[5] Rugar, D., Züger, O., Hoen, S., Yannoni, C. S., Vieth, H., and Kendrick, R. D. Force detection of nuclear magnetic resonance. *Science*, 264(5165):1560–1563, 1994.

[6] Stowe, T. D., Yasumura, K., Kenny, T. W., Botkin, D., Wago, K., and Rugar, D. Attonewton force detection using ultrathin silicon cantilevers. *Appl. Phys. Lett.*, 71(2):288–290, 1997.

[7] Chui, B. W., Hishinuma, Y., Budakian, R., Mamin, H. J., Kenny, T. W., and Rugar, D. Mass-loaded cantilevers with suppressed higher-order modes for magnetic resonance force microscopy. In *TRANSDUCERS, Solid-State Sensors, Actuators and Microsystems, 12th International Conference on, 2003*, volume 2, pages 1120–1123. IEEE, 2003.

[8] Wago, K., Botkin, D., Yannoni, C. S., and Rugar, D. Force-detected electron-spin resonance: Adiabatic inversion, nutation, and spin echo. *Phys. Rev. B*, 57 (2):1108, 1998.

[9] Stipe, B. C., Mamin, H. J., Yannoni, C. S., Stowe, T. D., Kenny, T. W., and Rugar, D. Electron spin relaxation near a micron-size ferromagnet. *Phys. Rev. Lett.*, 87(27):277602, 2001.

[10] Mamin, H. J., Budakian, R., Chui, B. W., and Rugar, D. Detection and manipulation of statistical polarization in small spin ensembles. *Phys. Rev. Lett.*, 91(20):207604, 2003.

[11] Garner, S. R., Kuehn, S., Dawlaty, J. M., Jenkins, N. E., and Marohn, J. A.

Force-gradient detected nuclear magnetic resonance. *Appl. Phys. Lett.*, 84(25): 5091–5093, 2004.

[12] Rugar, D., Budakian, R., Mamin, H. J., and Chui, B. W. Single spin detection by magnetic resonance force microscopy. *Nature*, 430(6997):329, 2004.

[13] Mamin, H. J., Budakian, R., Chui, B. W., and Rugar, D. Magnetic resonance force microscopy of nuclear spins: Detection and manipulation of statistical polarization. *Phys. Rev. B*, 72(2):024413, 2005.

[14] Mamin, H. J., Poggio, M., Degen, C. L., and Rugar, D. Nuclear magnetic resonance imaging with 90-nm resolution. *Nature Nanotechnol.*, 2(5):301, 2007.

[15] Mamin, H. J., Oosterkamp, T. H., Poggio, M., Degen, C. L., Rettner, C. T., and Rugar, D. Isotope-selective detection and imaging of organic nanolayers. *Nano Lett.*, 9(8):3020–3024, 2009.

[16] Degen, C. L., Poggio, M., Mamin, H. J., Rettner, C. T., and Rugar, D. Nanoscale magnetic resonance imaging. *Proc. Natl. Academy Sci.*, 106(5):1313–1317, 2009.

[17] Rose, W., Haas, H., Chen, A. Q., Jeon, N., Lauhon, L. J., Cory, D. G., and Budakian, R. High-resolution nanoscale solid-state nuclear magnetic resonance spectroscopy. *Phys. Rev. X*, 8(1):011030, 2018.

[18] Wago, K., Botkin, D., Yannoni, C. S., and Rugar, D. Paramagnetic and ferromagnetic resonance imaging with a tip-on-cantilever magnetic resonance force microscope. *Appl. Phys. Lett.*, 72(21):2757–2759, 1998.

[19] Bruland, K. J., Dougherty, W. M., Garbini, J. L., Sidles, J. A., and Chao, S. H. Force-detected magnetic resonance in a field gradient of 250 000 tesla per meter. *Appl. Phys. Lett.*, 73(21):3159–3161, 1998.

[20] Bartesaghi, A. and Subramaniam, S. Membrane protein structure determination using cryo-electron tomography and 3d image averaging. *Curr. Opin. Struct. Biol.*, 19(4):402–407, 2009.

[21] Zhou, Z. H. Atomic resolution cryo electron microscopy of macromolecular complexes. In *Advances in protein chemistry and structural biology*, volume 82, pages 1–35. *Elsevier*, 2011.

[22] Geelen, D., Thete, A., Schaff, O., Kaiser, A., van der Molen, S. J., and Tromp, R. eV-TEM: Transmission electron microscopy in a low energy cathode lens instrument. *Ultramicroscopy*, 159:482–487, 2015.

[23] Crowther, R. A. The Resolution Revolution: Recent Advances in CryoEM, volume 579. *Academic Press*, 2016.

[24] Murata, K. and Wolf, M. Cryo-electron microscopy for structural analysis of dynamic biological macromolecules. *Biochimica et Biophysica Acta (BBA)-General Subjects*, 1862(2):324–334, 2018.

[25] Maletinsky, P., Hong, S., Grinolds, M. S., Hausmann, B., Lukin, M. D.,

Walsworth, R. L., Loncar, M., and Yacoby, A. A robust scanning diamond sensor for nanoscale imaging with single nitrogen-vacancy centres. *Nature Nanotechnol.*, 7(5):320, 2012.

[26] Mamin, H. J., Kim, M., Sherwood, M. H., Rettner, C. T., Ohno, K., Awschalom, D. D., and Rugar, D. Nanoscale nuclear magnetic resonance with a nitrogen-vacancy spin sensor. *Science*, 339(6119):557–560, 2013.

[27] Müller, C., Kong, X., Cai, J.-M., Melentijević, K., Stacey, A., Markham, M., Twitchen, D., Isoya, J., Pezzagna, S., Meijer, J., Du, J. F., Plenio, M. B., Naydenov, B., McGuinness, L. P., and Jelezko, F. Nuclear magnetic resonance spectroscopy with single spin sensitivity. *Nature Commun.*, 5:4703, 2014.

[28] Zhang, Z., Hammel, P. C., and Wigen, P. E. Observation of ferromagnetic resonance in a microscopic sample using magnetic resonance force microscopy. *Appl. Phys. Lett.*, 68(14):2005–2007, 1996.

[29] Obukhov, Y., Pelekhov, D. V., Kim, J., Banerjee, P., Martin, I., Nazaretski, E., Movshovich, R., An, S., Gramila, T. J., Batra, S., and Hammel, P. C. Local ferromagnetic resonance imaging with magnetic resonance force microscopy. *Phys. Rev. Lett.*, 100(19):197601, 2008.

[30] Lee, I., Obukhov, Y., Xiang, G., Hauser, A., Yang, F., Banerjee, P., Pelekhov, D. V., and Hammel, P. C. Nanoscale scanning probe ferromagnetic resonance imaging using localized modes. *Nature*, 466(7308):845, 2010.

[31] Kinoshita, Y., Li, Y. J., Yoshimura, S., Saito, H., and Sugawara, Y. Magnetic resonance force microscopy using ferromagnetic resonance of a magnetic tip excited by microwave transmission via a coaxial resonator. *Nanotechnol.*, 28 (48):485709, 2017.

[32] Budakian, R., Mamin, H. J., and Rugar, D. Suppression of spin diffusion near a micron-size ferromagnet. *Phys. Rev. Lett.*, 92(3):037205, 2004.

[33] Cardellino, J., Scozzaro, N., Herman, M., Berger, A. J., Zhang, C., Fong, K. C., Jayaprakash, C., Pelekhov, D. V., and Hammel, P. C. The effect of spin transport on spin lifetime in nanoscale systems. *Nature Nanotechnol.*, 9(5):343–347, 2014.

[34] de Wit, M., Welker, G., de Voogd, J. M., and Oosterkamp, T. H. Density and t_1 of surface and bulk spins in diamond in high magnetic field gradients. *Phys. Rev. Appl.*, 10(6):064045, 2017.

[35] Alexson, D. A., Hickman, S. A., Marohn, J. A., and Smith, D. D. Single-shot nuclear magnetization recovery curves with force-gradient detection. *Appl. Phys. Lett.*, 101(2):022103, 2012.

[36] Saun, S.-B., Won, S., Kwon, S., and Lee, S. NMR spin-lattice relaxation time t1 of thin films obtained by magnetic resonance force microscopy. *J. Magn. Reson.*, 254:71–74, 2015.

[37] Wagenaar, J. J. T., den Haan, A. M. J., de Voogd, J. M., Bossoni, L., de Jong, T. A., de Wit, M., Bastiaans, K. M., Thoen, D. J., Endo, A., Klapwijk, T. M., Zaanen, J., and Oosterkamp, T. H. Probing the nuclear spin-lattice relaxation time at the nanoscale. *Phys. Rev. Appl.*, 6(1):014007, 2016.

[38] Wagenaar, J. J. T. Magnetic resonance force microscopy for condensed matter. PhD thesis, Leiden University, 2017.

[39] Bertero, M. and Boccacci, P. Introduction to inverse problems in imaging. *CRC press, Boca Raton, Florida, USA*, 1998.

[40] Nguyen, H. L. and Marohn, J. A. Reverse Monte Carlo reconstruction of electron spin-label coordinates from scanned-probe magnetic resonance microscope signals. *arXiv preprint*, 2018.

[41] Longenecker, J. G., Mamin, H. J., Senko, A. W., Chen, L., Rettner, C. T., Rugar, D., and Marohn, J. A. High-gradient nanomagnets on cantilevers for sensitive detection of nuclear magnetic resonance. *ACS Nano*, 6(11):9637–9645, 2012.

[42] Tao, Y. Nanomechanical systems with small dissipation. PhD thesis, Massachusetts Institute of Technology, 2016.

[43] Moores, B. A. J. Spanning the unbridged imaging regime: Advances in mechanically detected MRI. PhD thesis, ETH Zurich, 2015.

[44] Poggio, M., Degen, C. L., Mamin, H. J., and Rugar, D. Feedback cooling of a cantilevers fundamental mode below 5 mk. *Phys. Rev. Lett.*, 99(1):017201, 2007.

[45] Héritier, M., Eichler, A., Pan, Y., Grob, U., Shorubalko, I., Krass, M. D., Tao, Y., and Degen, C. L. Nanoladder cantilevers made from diamond and silicon. *Nano Lett.*, 18(3):1814–1818, 2018.

[46] De Bonis, S. L., Urgell, C., Yang, W., Samanta, C., Noury, A., Vergara-Cruz, J., Dong, Q., Jin, Y., and Bachtold, A. Ultrasensitive displacement noise measurement of carbon nanotube mechanical resonators. *Nano Lett.*, 18(8):5324–5328, 2018.

[47] Usenko, O., Vinante, A., Wijts, G. H. C. J., and Oosterkamp, T. H. A superconducting quantum interference device based read-out of a subattonewton force sensor operating at millikelvin temperatures. *Appl. Phys. Lett.*, 98(13): 133105, 2011.

[48] Vinante, A., Kirste, A., den Haan, A. M. J., Usenko, O., Wijts, G. H. C. J., Jeffrey, E., Sonin, P., Bouwmeester, D., and Oosterkamp, T. H. High sensitivity SQUID-detection and feedback-cooling of an ultrasoft microcantilever. *Appl. Phys. Lett.*, 101(12):123101, 2012.

[49] Vinante, A., Wijts, G. H. C. J., Usenko, O., Schinkelshoek, L., and Oosterkamp, T. H. Magnetic resonance force microscopy of paramagnetic electron spins at

millikelvin temperatures. *Nature Commun.*, 2:572, 2011.

[50] Wagenaar, J. J. T., den Haan, A. M. J., Donkersloot, R. J., Marsman, F., de Wit, M., Bossoni, L., and Oosterkamp, T. H. Mechanical generation of radio-frequency fields in nuclear-magnetic-resonance force microscopy. *Phys. Rev. Appl.*, 7(2):024019, 2018.

[51] den Haan, A. M. J., Wagenaar, J. J. T., de Voogd, J. M., Koning, G., and Oosterkamp, T. H. Spin-mediated dissipation and frequency shifts of a cantilever at milliKelvin temperatures. *Phys. Rev. B*, 92(23):235441, dec 2015.

[52] De Voogd, J. M., Wagenaar, J. J. T., and Oosterkamp, T. H. Dissipation and resonance frequency shift of a resonator magnetically coupled to a semiclassical spin. *Sci. Rep.*, 7:42239, February 2017. ISSN 2045-2322.

[53] Wijts, G. H. C. J. Magnetic resonance force microscopy at milliKelvin temperatures. PhD thesis, Leiden University, 2013.

[54] den Haan, A. M. J. Nuclear magnetic resonance force microscopy at milliKelvin temperatures. PhD thesis, Leiden University, 2016.

[55] Thoen, D. J., Bos, B. G. C., Haalebos, E. A. F., Klapwijk, T. M., Baselmans, J. J. A., and Endo, A. Superconducting NbTiN thin films with highly uniform properties over a ∅ 100 mm wafer. *IEEE T. on Appl. Supercond.*, 27(4):1–5, 2017.

[56] Klimov, A., Słysz, W., Guziewicz, M., Kolkovsky, V., Zaytseva, I., and Malinowski, A. Characterization of the critical current and physical properties of superconducting epitaxial NbTiN sub-micron structures. *Physica C: Supercond. its Appl.*, 536:35–38, 2017.

[57] Poggio, M., Degen, C. L., Rettner, C. T., Mamin, H. J., and Rugar, D. Nuclear magnetic resonance force microscopy with a microwire rf source. *Appl. Phys. Lett.*, 90(26):263111, 2007.

[58] Griffiths, D. J. Introduction to Electrodynamics, Third Edition, International Edition. *Pearson Benjamin Cummings*, 2008.

[59] de Voogd, J. M. Magnetic resonance force microscopy and the spin bath. PhD thesis, Leiden University, 2017.

[60] Cleveland, J. P., Manne, S., Bocek, D., and Hansma, P. K. A nondestructive method for determining the spring constant of cantilevers for scanning force microscopy. *Rev. Sci. Instruments*, 64(2):403–405, 1993.

[61] MEMSnet. material: Silicon (si), bulk. URL `https://www.memsnet.org/material/siliconsibulk/`.

[62] Sidles, J. A., Garbini, J. L., Bruland, K. J., Rugar, D., Züger, O., Hoen, S., and Yannoni, C. S. Magnetic resonance force microscopy. *Reviews Mod. Phys.*, 67(1):249, 1995.

[63] Mamin, H. J., Budakian, R., and Rugar, D. Superconducting microwave res-

onator for millikelvin magnetic resonance force microscopy. *Rev. Sci. Instruments*, 74(5):2749–2753, 2003.

[64] Yuan, M., Cohen, M. A., and Steele, G. A. Silicon nitride membrane resonators at millikelvin temperatures with quality factors exceeding 108. *Appl. Phys. Lett.*, 107(26):263501, 2015.

[65] Opdam, D. Characterization of silicon nitride cantilevers and mechanical feedback cooling. Master's thesis, Leiden University, 2018.

[66] Jones, M. H. and Jones, S. H. The general properties of si, ge, sige, sio_2 and si_3n_4. *Virginia Semiconductor Inc.*, 2002.

[67] van Velzen, M. New methods to improve the usability in magnetic resonance frequency microscopy. Master's thesis, Leiden University, 2018.

[68] Yazdanian, S. M., Marohn, J. A., and Loring, R. F. Dielectric fluctuations in force microscopy: Noncontact friction and frequency jitter. *The J. Chem. Phys.*, 128(22):224706, 2008.

[69] Heeres, E. C., Katan, A. J., Van Es, M. H., Beker, A. F., Hesselberth, M., van Der Zalm, D. J., and Oosterkamp, T. H. A compact multipurpose nanomanipulator for use inside a scanning electron microscope. *Rev. Sci. Instruments*, 81 (2):023704, 2010.

[70] Nazaretski, E., Pelekhov, D. V., Martin, I., Zalalutdinov, M., Ponarin, D., Smirnov, A., Hammel, P. C., and Movshovich, R. Detection of localized ferromagnetic resonance in a continuous thin film via magnetic resonance force microscopy. *Phys. Rev. B*, 79(13):132401, 2009.

[71] Berman, G. P., Borgonovi, F., Gorshkov, V. N., and Tsifrinovich, V. I. Modeling and simulations of a single-spin measurement using mrfm. *IEEE T. on Nanotechnol.*, 4(1):14–20, 2005.

[72] Petersan, P. J. and Anlage, S. M. Measurement of resonant frequency and quality factor of microwave resonators: Comparison of methods. *J. Appl. Phys.*, 84(6):3392–3402, 1998.

[73] JPE. Jpe - cryogenic linear actuator "piezoknob", 2018. URL `https://www.janssenprecisionengineering.com`.

[74] Bian, L., Wen, Y., Li, P., Wu, Y., Zhang, X., and Li, M. Magnetostrictive stress induced frequency shift in resonator for magnetic field sensor. *Sens. Actuator. A: Phys.*, 247:453–458, 2016.

[75] De Waele, A. T. A. M. Basic operation of cryocoolers and related thermal machines. *J. Low Temp. Phys.*, 164(5-6):179, 2011.

[76] Chijioke, A. and Lawall, J. Vibration spectrum of a pulse-tube cryostat from 1hz to 20khz. *Cryogenics*, 50(4):266–270, 2010.

[77] Den Haan, A. M. J., Wijts, G. H. C. J., Galli, F., Usenko, O., Van Baarle, G. J. C., Van Der Zalm, D. J., and Oosterkamp, T. H. Atomic resolution scanning

tunneling microscopy in a cryogen free dilution refrigerator at 15 mk. *Rev. Sci. Instruments*, 85(3):035112, 2014.

[78] Pan, S. H., Hudson, E. W., and Davis, J. C. ^{3}He refrigerator based very low temperature scanning tunneling microscope. *Rev. Sci. Instruments*, 70(2):1459–1463, 1999.

[79] Moussy, N., Courtois, H., and Pannetier, B. A very low temperature scanning tunneling microscope for the local spectroscopy of mesoscopic structures. *Rev. Sci. Instruments*, 72(1):128–131, 2001.

[80] Wiebe, J., Wachowiak, A., Meier, F., Haude, D., Foster, T., Morgenstern, M., and Wiesendanger, R. A 300 mk ultra-high vacuum scanning tunneling microscope for spin-resolved spectroscopy at high energy resolution. *Rev. Sci. Instruments*, 75(11):4871–4879, 2004.

[81] Kambara, H., Matsui, T., Niimi, Y., and Fukuyama, H. Construction of a versatile ultralow temperature scanning tunneling microscope. *Rev. Sci. Instruments*, 78(7):073703, 2007.

[82] Marz, M., Goll, G., and Löhneysen, H. v. A scanning tunneling microscope for a dilution refrigerator. *Rev. Sci. Instruments*, 81(4):045102, 2010.

[83] Song, Y. J., Otte, A. F., Shvarts, V., Zhao, Z., Kuk, Y., Blankenship, S. R., Band, A., Hess, F. M., and Stroscio, J. A. Invited review article: A 10 mk scanning probe microscopy facility. *Rev. Sci. Instruments*, 81(12):121101, 2010.

[84] Misra, S., Zhou, B. B., Drozdov, I. K., Seo, J., Urban, L., Gyenis, A., Kingsley, S. C. J., Jones, H., and Yazdani, A. Design and performance of an ultra-high vacuum scanning tunneling microscope operating at dilution refrigerator temperatures and high magnetic fields. *Rev. Sci. Instruments*, 84(10):103903, 2013.

[85] Singh, U. R., Enayat, M., White, S. C., and Wahl, P. Construction and performance of a dilution-refrigerator based spectroscopic-imaging scanning tunneling microscope. *Rev. Sci. Instruments*, 84(1):013708, 2013.

[86] Roychowdhury, A., Gubrud, M. A., Dana, R., Anderson, J. R., Lobb, C. J., Wellstood, F. C., and Dreyer, M. A 30 mk, 13.5 t scanning tunneling microscope with two independent tips. *Rev. Sci. Instruments*, 85(4):043706, 2014.

[87] von Allwörden, H., Eich, A., Knol, E. J., Hermenau, J., Sonntag, A., Gerritsen, J. W., Wegner, D., and Khajetoorians, A. A. Design and performance of an ultra-high vacuum spin-polarized scanning tunneling microscope operating at 30 mk and in a vector magnetic field. *Rev. Sci. Instruments*, 89(3):033902, 2018.

[88] Machida, T., Kohsaka, Y., and Hanaguri, T. A scanning tunneling microscope for spectroscopic imaging below 90 mk in magnetic fields up to 17.5 t. *Rev. Sci. Instruments*, 89(9):093707, 2018.

[89] Battisti, I., Verdoes, G., van Oosten, K., Bastiaans, K. M., and Allan, M. P.

Definition of design guidelines, construction, and performance of an ultra-stable scanning tunneling microscope for spectroscopic imaging. *Rev. Sci. Instruments*, 89(12):123705, 2018.

[90] Pelekhov, D. V., Becker, J. B., and Nunes Jr, G. Ultralow-temperature atomic force microscopy for the investigation of mesoscopic systems. *Appl. Phys. Lett.*, 72(8):993–995, 1998.

[91] Gildemeister, A. E., Ihn, T., Barengo, C., Studerus, P., and Ensslin, K. Construction of a dilution refrigerator cooled scanning force microscope. *Rev. Sci. Instruments*, 78(1):013704, 2007.

[92] Mamin, H. J. and Rugar, D. Sub-attonewton force detection at millikelvin temperatures. *Appl. Phys. Lett.*, 79(20):3358–3360, 2001.

[93] Björnsson, P. G., Gardner, B. W., Kirtley, J. R., and Moler, K. A. Scanning superconducting quantum interference device microscope in a dilution refrigerator. *Rev. Sci. Instruments*, 72(11):4153–4158, 2001.

[94] Seo, Y., Cadden-Zimansky, P., and Chandrasekhar, V. Low-temperature high-resolution magnetic force microscopy using a quartz tuning fork. *Appl. Phys. Lett.*, 87(10):103103, 2005.

[95] Schaefer-Nolte, E., Reinhard, F., Ternes, M., Wrachtrup, J., and Kern, K. A diamond-based scanning probe spin sensor operating at low temperature in ultra-high vacuum. *Rev. Sci. Instruments*, 85(1):013701, 2014.

[96] Halbertal, D., Cuppens, J., Shalom, M. B., Embon, L., Shadmi, N., Anahory, Y., Naren, H., Sarkar, J., Uri, A., Ronen, Y., Myasoedov, Y., Levitov, L. S., Joselevich, E., Geim, A. K., and Zeldov, E. Nanoscale thermal imaging of dissipation in quantum systems. *Nature*, 539(7629):407, 2016.

[97] Kleckner, D. and Bouwmeester, D. Sub-kelvin optical cooling of a micromechanical resonator. *Nature*, 444(7115):75, 2006.

[98] Bassi, A., Lochan, K., Satin, S., Singh, T. P., and Ulbricht, H. Models of wavefunction collapse, underlying theories, and experimental tests. *Reviews Mod. Phys.*, 85(2):471, 2013.

[99] Binnig, G., Rohrer, H., Gerber, C., and Weibel, E. Tunneling through a controllable vacuum gap. *Appl. Phys. Lett.*, 40(2):178–180, 1982.

[100] Olivieri, E., Billard, J., De Jesus, M., Juillard, A., and Leder, A. Vibrations on pulse tube based dry dilution refrigerators for low noise measurements. *Nucl. Instruments Methods Phys. Res. Section A: Accelerators, Spectrometers, Detectors Associated Equipment*, 858:73–79, 2017.

[101] Davidsson, P., Olin, H., Persson, M., and Pehrson, S. Design and operation of a low-temperature scanning tunneling microscope suitable for operation below 1 k. *Ultramicroscopy*, 42:1470–1475, 1992.

[102] Ast, C. R., Assig, M., Ast, A., and Kern, K. Design criteria for scanning tun-

neling microscopes to reduce the response to external mechanical disturbances. *Rev. Sci. Instruments*, 79(9):093704, 2008.

[103] Foley, E. T., Yoder, N. L., Guisinger, N. P., and Hersam, M. C. Cryogenic variable temperature ultrahigh vacuum scanning tunneling microscope for single molecule studies on silicon surfaces. *Rev. Sci. Instruments*, 75(12):5280–5287, 2004.

[104] Caparrelli, S., Majorana, E., Moscatelli, V., Pascucci, E., Perciballi, M., Puppo, P., Rapagnani, P., and Ricci, F. Vibration-free cryostat for low-noise applications of a pulse tube cryocooler. *Rev. Sci. Instruments*, 77(9):095102, 2006.

[105] Pelliccione, M., Sciambi, A., Bartel, J., Keller, A. J., and Goldhaber-Gordon, D. Design of a scanning gate microscope for mesoscopic electron systems in a cryogen-free dilution refrigerator. *Rev. Sci. Instruments*, 84(3):033703, 2013.

[106] Poggio, M. and Degen, C. L. Force-detected nuclear magnetic resonance: recent advances and future challenges. *Nanotechnol.*, 21(34):342001, 2010.

[107] Fowles, G. R. and Cassiday, G. L. Analytical mechanics, 7th edition. *Thomson Learning, inc.*, 2005.

[108] Campbell. Electrical receiving, translating, or repeating circuit, 1917.

[109] Pobell, F. Matter and methods at low temperatures. *Springer Science & Business Media*, 2007.

[110] Woodcraft, A. L. Recommended values for the thermal conductivity of aluminium of different purities in the cryogenic to room temperature range, and a comparison with copper. *Cryogenics*, 45(9):626–636, 2005.

[111] Aspelmeyer, M., Kippenberg, T. J., and Marquardt, F. Cavity optomechanics. *Reviews Mod. Phys.*, 86(4):1391, 2014.

[112] Vinante, A., Bahrami, M., Bassi, A., Usenko, O., Wijts, G. H. C. J., and Oosterkamp, T. H. Upper bounds on spontaneous wave-function collapse models using millikelvin-cooled nanocantilevers. *Phys. Rev. Lett.*, 116(9):090402, 2016.

[113] Chen, L., Longenecker, J. G., Moore, E. W., and Marohn, J. A. Long-lived frequency shifts observed in a magnetic resonance force microscope experiment following microwave irradiation of a nitroxide spin probe. *Appl. Phys. Lett.*, 102 (13):132404, 2013.

[114] Nichol, J. M., Hemesath, E. R., Lauhon, L. J., and Budakian, R. Nanomechanical detection of nuclear magnetic resonance using a silicon nanowire oscillator. *Phys. Rev. B*, 85(5):054414, 2012.

[115] Meyer, E. S., Silvera, I. F., and Brandt, B. L. Eddy current shielding and heating: Reduction of dissipation for very low-temperature experiments in the presence of magnetic field ripple. *Rev. Sci. Instruments*, 60(9):2964–2968, 1989.

[116] Isaac, C. E., Gleave, C. M., Nasr, P. T., Nguyen, H. L., Curley, E. A., Yoder, J. L., Moore, E. W., Chen, L., and Marohn, J. A. Dynamic nuclear polarization

in a magnetic resonance force microscope experiment. *Phys. Chem. Chem. Phys.*, 18(13):8806–8819, 2016.

[117] Abragam, A. Principles of nuclear magnetism (International series of monographs on physics). *Clarendon Press, Oxford*, 1961.

[118] Bloch, F. Nuclear induction. *Phys. Rev.*, 70(7-8):460, 1946.

[119] Slichter, C. P. Principles of Magnetic Resonance, volume 1 of Springer Series in Solid-State Sciences. *Springer Berlin Heidelberg, Berlin, Heidelberg*, 1990.

[120] Mulkern, R. V. and Williams, M. L. The general solution to the bloch equation with constant rf and relaxation terms: application to saturation and slice selection. *Med. Phys.*, 20(1):5–13, 1993.

[121] Murase, K. and Tanki, N. Numerical solutions to the time-dependent Bloch equations revisited. *Magn. Reson. Imaging*, 29(1):126–131, 2011.

[122] Herzog, B. E., Cadeddu, D., Xue, F., Peddibhotla, P., and Poggio, M. Boundary between the thermal and statistical polarization regimes in a nuclear spin ensemble. *Appl. Phys. Lett.*, 105(4):043112, 2014.

[123] Hoepker, N., Lekkala, S., Loring, R. F., and Marohn, J. A. Dielectric fluctuations over polymer films detected using an atomic force microscope. *The J. Phys. Chem. B*, 115(49):14493–14500, 2011.

[124] Yazdanian, S. M., Hoepker, N., Kuehn, S., Loring, R. F., and Marohn, J. A. Quantifying electric field gradient fluctuations over polymers using ultrasensitive cantilevers. *Nano Lett.*, 9(6):2273–2279, 2009.

[125] Moore, E. W., Lee, S., Hickman, S. A., Wright, S. J., Harrell, L. E., Borbat, P. P., Freed, J. H., and Marohn, J. A. Scanned-probe detection of electron spin resonance from a nitroxide spin probe. *Proc. Natl. Academy Sci.*, 106(52): 22251–22256, 2009.

[126] Oosterkamp, T. H., Poggio, M., Degen, C. L., Mamin, H. J., and Rugar, D. Frequency domain multiplexing of force signals with application to magnetic resonance force microscopy. *Appl. Phys. Lett.*, 96(8):083107, 2010.

[127] Moores, B. A. J., Eichler, A., Tao, Y., Takahashi, H., Navaretti, P., and Degen, C. L. Accelerated nanoscale magnetic resonance imaging through phase multiplexing. *Appl. Phys. Lett.*, 106(21):213101, 2015.

[128] Grapengeter, H. H., Kosfeld, R., and Offergeld, H. W. Influences of paramagnetic impurities on the proton spin-lattice relaxation time T_1 of siloxane polymers. *Polymer*, 21(7):829–831, 1980.

[129] Lounasmaa, O. V. Nuclear magnetism in copper, silver, and rhodium metals at positive and negative spin temperatures in the nano-and picokelvin regimes. *Matematisk-Fysiske Meddelelser*, pages 401–443, 1997.

[130] Oja, A. S. and Lounasmaa, O. V. Nuclear magnetic ordering in simple metals at positive and negative nanokelvin temperatures. *Reviews Mod. Phys.*, 69(1):

1, 1997.

[131] Bloembergen, N. On the interaction of nuclear spins in a crystalline lattice. *Physica*, 15(3-4):386–426, 1949.

[132] Ofori-Okai, B. K., Pezzagna, S., Chang, K., Loretz, M., Schirhagl, R., Tao, Y., Moores, B. A., Groot-Berning, K., Meijer, J., and Degen, C. L. Spin properties of very shallow nitrogen vacancy defects in diamond. *Phys. Rev. B*, 86(8): 081406, 2012.

[133] Rondin, L., Tetienne, J. P., Hingant, T., Roch, J. F., Maletinsky, P., and Jacques, V. Magnetometry with nitrogen-vacancy defects in diamond. *Rep. on Prog. Phys.*, 77(5):056503, 2014.

[134] Bar-Gill, N., Pham, L. M., Belthangady, C., Le Sage, D., Cappellaro, P., Maze, J. R., Lukin, M. D., Yacoby, A., and Walsworth, R. Suppression of spin-bath dynamics for improved coherence of multi-spin-qubit systems. *Nature Commun.*, 3:858, 2012.

[135] Myers, B. A., Das, A., Dartiailh, M. C., Ohno, K., Awschalom, D. D., and Bleszynski Jayich, A. C. Probing surface noise with depth-calibrated spins in diamond. *Phys. Rev. Lett.*, 113(2):027602, July 2014.

[136] Lee, D., Lee, K. W., Cady, J. V., Ovartchaiyapong, P., and Bleszynski Jayich, A. C. Topical review: Spins and mechanics in diamond. *J. Opt.*, 19(3):033001, 2017.

[137] Luan, L., Grinolds, M. S., Hong, S. K., Maletinsky, P., Walsworth, R. L., and Yacoby, A. Decoherence imaging of spin ensembles using a scanning single-electron spin in diamond. *Sci. Rep.*, 5:8119, January 2015.

[138] Romach, Y., Müller, C., Unden, T., Rogers, L. J., Isoda, T., Itoh, K. M., Markham, M., Stacey, A., Meijer, J., Pezzagna, S., Naydenov, B., McGuinness, L. P., Bar-Gill, N., and Jelezko, F. Spectroscopy of surface-induced noise using shallow spins in diamond. *Phys. Rev. Lett.*, 114(1):017601, jan 2015.

[139] Rosskopf, T., Dussaux, A., Ohashi, K., Loretz, M., Schirhagl, R., Watanabe, H., Shikata, S., Itoh, K. M., and Degen, C. L. Investigation of surface magnetic noise by shallow spins in diamond. *Phys. Rev. Lett.*, 112(14):147602, apr 2014.

[140] Grinolds, M. S., Warner, M., De Greve, K., Dovzhenko, Y., Thiel, L., Walsworth, R. L., Hong, S., Maletinsky, P., and Yacoby, A. Subnanometre resolution in three-dimensional magnetic resonance imaging of individual dark spins. *Nature Nanotechnol.*, 9(4):279–284, April 2014.

[141] Bruno, A., De Lange, G., Asaad, S., Van der Enden, K. L., Langford, N. K., and DiCarlo, L. Reducing intrinsic loss in superconducting resonators by surface treatment and deep etching of silicon substrates. *Appl. Phys. Lett.*, 106(18): 182601, 2015.

[142] Pappas, D. P., Vissers, M. R., Wisbey, D. S., Kline, J. S., and Gao, J. Two

level system loss in superconducting microwave resonators. *IEEE T. on Appl. Supercond.*, 21(3):871–874, 2011.

[143] Casola, F., van der Sar, T., and Yacoby, A. Probing condensed matter physics with magnetometry based on nitrogen-vacancy centres in diamond. *Nature Reviews Mater.*, 3:17088, 2018.

[144] Takahashi, S., Hanson, R., van Tol, J., Sherwin, M. S., and Awschalom, D. D. Quenching spin decoherence in diamond through spin bath polarization. *Phys. Rev. Lett.*, 101(4):047601, 2008.

[145] Peddibhotla, P., Xue, F., Hauge, H. I. T., Assali, S., Bakkers, E. P. A. M., and Poggio, M. Harnessing nuclear spin polarization fluctuations in a semiconductor nanowire. *Nature Phys.*, 9(10):631–635, 2013.

[146] Griffiths, D. J. Introduction to Electrodynamics, Third Edition. *Prentice Hall, Upper Saddle River*, 1999.

[147] Stipe, B. C., Mamin, H. J., Stowe, T. D., Kenny, T. W., and Rugar, D. Noncontact friction and force fluctuations between closely spaced bodies. *Phys. Rev. Lett.*, 87(9):096801, 2001.

[148] Kuehn, S., Loring, R. F., and Marohn, J. A. Dielectric fluctuations and the origins of noncontact friction. *Phys. Rev. Lett.*, 96(15):156103, 2006.

[149] Vinante, A., Mezzena, R., Falferi, P., Carlesso, M., and Bassi, A. Improved noninterferometric test of collapse models using ultracold cantilevers. *Phys. Rev. Lett.*, 119(11):110401, 2017.

[150] Koch, R. H., Foglietti, V., Rozen, J. R., Stawiasz, K. G., Ketchen, M. B., Lathrop, D. K., Sun, J. Z., and Gallagher, W. J. Effects of radio frequency radiation on the dc SQUID. *Appl. Phys. Lett.*, 65(1):100–102, 1994.

[151] Mück, M., Dechert, J., Gail, J., Kreutzbruck, M., Schöne, S., and Weidl, R. Response of radio frequency superconducting quantum interference devices to electromagnetic interference. *Rev. Sci. Instruments*, 66(9):4690–4693, 1995.

[152] Clarke, J. and Braginski, A. I. The SQUID handbook: Applications of SQUIDs and SQUID systems. *John Wiley & Sons*, 2006.

[153] Webb, R. A. New technique for improved low-temperature SQUID NMR measurements. *Rev. Sci. Instruments*, 48(12):1585–1594, 1977.

[154] Fan, N. Q., Heaney, M. B., Clarke, J., Newitt, D., Wald, L. L., Hahn, E. L., Bielecki, A., and Pines, A. Nuclear magnetic resonance with dc SQUID preamplifiers. *IEEE T. on Magn.*, 25(2):1193–1199, 1989.

[155] Greenberg, Y. S. Application of superconducting quantum interference devices to nuclear magnetic resonance. *Reviews Mod. Phys.*, 70(1):175, 1998.

[156] Clarke, J., Hatridge, M., and Mößle, M. SQUID-detected magnetic resonance imaging in microtesla fields. *Annu. Rev. Biomed. Eng.*, 9:389–413, 2007.

[157] Augustine, M. P., TonThat, D. M., and Clarke, J. SQUID detected NMR and NQR. *Solid State Nucl. Magn. Reson.*, 11(1-2):139–156, 1998.

[158] McDermott, R., Lee, S., Haken, B. t., Trabesinger, A. H., Pines, A., and Clarke, J. Microtesla magnetic resonance imaging with a superconducting quantum interference device. *Proc. Natl. Academy Sci.*, 101(21):7857–61, 2004.

[159] Matlachov, A. N., Volegov, P. L., Espy, M. A., George, J. S., and Kraus Jr, R. H. SQUID detected NMR in microtesla magnetic fields. *J. Magn. Reson.*, 170(1):1–7, 2004.

[160] Buckenmaier, K., Rudolph, M., Back, C., Misztal, T., Bommerich, U., Fehling, P., Koelle, D., Kleiner, R., Mayer, H. A., Scheffler, K., et al. SQUID-based detection of ultra-low-field multinuclear NMR of substances hyperpolarized using signal amplification by reversible exchange. *Sci. Rep.*, 7(1):13431, 2017.

[161] Ehnholm, G. J., Ekström, J. P., Loponen, M. T., and Soini, J. K. Transversal SQUID NMR. *Cryogenics*, 19(11):673–678, 1979.

[162] Pasquarelli, A., Del Gratta, C., Della Penna, S., Di Luzio, S., Pizzella, V., and Romani, G. L. A SQUID based AC susceptometer for the investigation of large samples. *Phys. Med. Biol.*, 41(11):2533, 1996.

[163] Pizzella, V., Della Penna, S., Del Gratta, C., and Romani, G. L. SQUID systems for biomagnetic imaging. *Supercond. Science Technol.*, 14(7):R79, 2001.

[164] Quantum Design Inc. SQUID application note 1052-202a: Coupling magnetic signals to a SQUID amplifier, October 2001. URL `https://www.qdusa.com/sitedocs/appNotes/squids/1052-202.pdf`.

[165] Garwood, M. and DelaBarre, L. The return of the frequency sweep: designing adiabatic pulses for contemporary NMR. *J. Magn. Reson.*, 153(2):155–177, 2001.

[166] O'Dell, L. A. The WURST kind of pulses in solid-state NMR. *Solid State Nucl. Magn. Reson.*, 55:28–41, 2013.

[167] Claridge, T. D. W. High-resolution NMR techniques in organic chemistry, volume 27. *Elsevier*, 2016.

[168] Fagaly, R. Superconducting quantum interference device instruments and applications. *Rev. Sci. Instruments*, 77(10):101101, 2006.

[169] Choi, W. S., Kim, M. J., Jeong, I. W., Kim, D. E., Park, H. C., and Park, K. H. Development of high-stability magnet power supply. *Nucl. Instruments Methods Phys. Res. A: Accelerators, Spectrometers, Detectors Associated Equipment*, 822:15–24, 2016.

[170] van Waarde, B., Benningshof, O. W. B., and Oosterkamp, T. H. A magnetic persistent current switch at millikelvin temperatures. *Cryogenics*, 78:74–77, 2016.

[171] Hortensius, H. L., Driessen, E. F. C., Klapwijk, T. M., Berggren, K. K., and

Clem, J. R. Critical-current reduction in thin superconducting wires due to current crowding. *Appl. Phys. Lett.*, 100(18):182602, 2012.

[172] Stoll, R. L. The analysis of eddy currents. *Clarendon Press*, 1974.

[173] Popovic, Z. and Popovic, B. D. Introductory electromagnetics. *Prentice hall Upper Saddle River, NJ, USA:*, 2000.

[174] Duthil, P. Material properties at low temperature. *arXiv preprint arXiv:1501.07100*, 2015.

[175] Tinkham, M. Introduction to superconductivity. *Courier Corporation*, 2004.

[176] Annett, J. F. Superconductivity, superfluids and condensates, volume 5. *Oxford University Press*, 2004.

[177] Driessen, E. F. C., Coumou, P. C. J. J., Tromp, R. R., De Visser, P. J., and Klapwijk, T. M. Strongly disordered TiN and NbTiN s-wave superconductors probed by microwave electrodynamics. *Phys. Rev. Lett.*, 109(10):107003, 2012.

[178] Abrikosov, A. A. On the magnetic properties of second kind superconductors. *Sov. Phys. JETP*, 5(6):1174–1182, 1957.

[179] Kim, Y. B., Hempstead, C. F., and Strnad, A. R. Flux-flow resistance in type-II superconductors. *Phys. Rev.*, 139(4A):A1163, 1965.

[180] Embon, L., Anahory, Y., Suhov, A., Halbertal, D., Cuppens, J., Yakovenko, A., Uri, A., Myasoedov, Y., Rappaport, M. L., Huber, M. E., Gurevich, A., and Zeldov, E. Probing dynamics and pinning of single vortices in superconductors at nanometer scales. *Sci. Rep.*, 5:7598, 2015.

[181] Raes, B., Van de Vondel, J., Silhanek, A. V., de Souza Silva, C. C., Gutierrez, J., Kramer, R. B. G., and Moshchalkov, V. V. Local mapping of dissipative vortex motion. *Phys. Rev. B*, 86(6):064522, 2012.

[182] Bardeen, J. and Stephen, M. J. Theory of the motion of vortices in superconductors. *Phys. Rev.*, 140(4A):A1197, 1965.

[183] Yu, L., Newman, N., and Rowell, J. M. Measurement of the coherence length of sputtered NbTiN thin films. *IEEE T. on Appl. Supercond.*, 12(2):1795–1798, 2002.

[184] Yu, L., Singh, R. K., Liu, H., Wu, S. Y., Hu, R., Durand, D., Bulman, J., Rowell, J. M., and Newman, N. Fabrication of niobium titanium nitride thin films with high superconducting transition temperatures and short penetration lengths. *IEEE T. on Appl. Supercond.*, 15(1):44–48, 2005.

[185] Wilde, S., Valizadeh, R., Malyshev, O. B., Stenning, G. B. G., Hannah, A., Pattalwar, S., Pattalwar, N., Barradas, N. P., Alves, E., and Chesca, B. Physical vapour deposition of NbTiN thin films for superconducting RF cavities. *Loughborough University Institutional Repository*, 2017.

[186] Stan, G., Field, S. B., and Martinis, J. M. Critical field for complete vortex

expulsion from narrow superconducting strips. *Phys. Rev. Lett.*, 92(9):097003, 2004.

[187] Gurevich, A. Enhancement of rf breakdown field of superconductors by multilayer coating. *Appl. Phys. Lett.*, 88(1):012511, 2006.

[188] Haugan, T., Barnes, P. N., Wheeler, R., Meisenkothen, F., and Sumption, M. Addition of nanoparticle dispersions to enhance flux pinning of the $YBa_2Cu_3O_{7-x}$ superconductor. *Nature*, 430(7002):867, 2004.

[189] Maiorov, B., Baily, S. A., Zhou, H., Ugurlu, O., Kennison, J. A., Dowden, P. C., Holesinger, T. G., Foltyn, S. R., and Civale, L. Synergetic combination of different types of defect to optimize pinning landscape using $BaZrO_3$-doped $YBa_2Cu_3O_7$. *Nature Mater.*, 8(5):398, 2009.

[190] Fang, L., Jia, Y., Mishra, V., Chaparro, C., Vlasko-Vlasov, V. K., Koshelev, A. E., Welp, U., Crabtree, G. W., Zhu, S., Zhigadlo, N. D., Katrych, S., Karpinski, J., and Kwok, W. K. Huge critical current density and tailored superconducting anisotropy in $SmFeAsO_{0.8}F_{0.15}$ by low-density columnar-defect incorporation. *Nature Commun.*, 4:2655, 2013.

[191] Córdoba, R., Baturina, T. I., Sesé, J., Mironov, A. Y., De Teresa, J. M., Ibarra, M. R., Nasimov, D. A., Gutakovskii, A. K., Latyshev, A. V., Guillamón, I., Suderow, H., Vieira, S., Baklanov, M. R., Palacios, J. J., and M., V. V. Magnetic field-induced dissipation-free state in superconducting nanostructures. *Nature Commun.*, 4:1437, 2013.

[192] Wang, Y.-L., Glatz, A., Kimmel, G. J., Aranson, I. S., Thoutam, L. R., Xiao, Z.-L., Berdiyorov, G. R., Peeters, F. M., Crabtree, G. W., and Kwok, W.-K. Parallel magnetic field suppresses dissipation in superconducting nanostrips. *Proc. Natl. Academy Sci.*, 114(48):E10274–E10280, 2017.

[193] Barends, R., Hortensius, H. L., Zijlstra, T., Baselmans, J. J. A., Yates, S. J. C., Gao, J. R., and Klapwijk, T. M. Contribution of dielectrics to frequency and noise of nbtin superconducting resonators. *Appl. Phys. Lett.*, 92(22):223502, 2008.

[194] Bruno, A., Skacel, S. T., Kaiser, C., Wünsch, S., Siegel, M., Ustinov, A. V., and Lisitskiy, M. P. Investigation of dielectric losses in hydrogenated amorphous-silicon (a-si: H) thin films using superconducting microwave resonators. *Phys. Procedia*, 36:245–249, 2012.

[195] Calusine, G., Melville, A., Woods, W., Das, R., Stull, C., Bolkhovsky, V., Braje, D., Hover, D., Kim, D. K., Miloshi, X., et al. Analysis and mitigation of interface losses in trenched superconducting coplanar waveguide resonators. *Appl. Phys. Lett.*, 112(6):062601, 2018.

[196] Rosenberg, H. M. The thermal conductivity of germanium and silicon at low temperatures. *Proc. Phys. Soc. Section A*, 67(9):837, 1954.

[197] Mamin, H. J., Rettner, C. T., Sherwood, M. H., Gao, L., and Rugar, D. High field-gradient dysprosium tips for magnetic resonance force microscopy. *Appl. Phys. Lett.*, 100(1):013102, 2012.

[198] Nichol, J. M., Naibert, T. R., Hemesath, E. R., Lauhon, L. J., and Budakian, R. Nanoscale Fourier-transform magnetic resonance imaging. *Phys. Rev. X*, 3 (3):031016, 2013.

[199] Fong, K. C., Herman, M. R., Banerjee, P., Pelekhov, D. V., and Hammel, P. C. Spin lifetime in small ensembles of electron spins measured by magnetic resonance force microscopy. *Phys. Rev. B*, 84(22):220405, 2011.

[200] Campanella, H., Del Real, R. P., Díaz-Michelena, M., Duch, M., Guerrero, H., Esteve, J., and Plaza, J. A. Focused-ion-beam-assisted magnet fabrication and manipulation for magnetic field detection applications. *ACS Appl. Mater. & Interfaces*, 1(3):527–531, 2009.

[201] Overweg, H. C., Den Haan, A. M. J., Eerkens, H. J., Alkemade, P. F. A., La Rooij, A. L., Spreeuw, R. J. C., Bossoni, L., and Oosterkamp, T. H. Probing the magnetic moment of FePt micromagnets prepared by focused ion beam milling. *Appl. Phys. Lett.*, 107(7):072402, 2015.

[202] Longenecker, J. G., Moore, E. W., and Marohn, J. A. Rapid serial prototyping of magnet-tipped attonewton-sensitivity cantilevers by focused ion beam manipulation. *J. Vac. Science & Technol. B, Nanotechnol. Microelectronics: Materials, Processing, Measurement, Phenom.*, 29(3):032001, 2011.

[203] Hickman, S. A., Moore, E. W., Lee, S., Longenecker, J. G., Wright, S. J., Harrell, L. E., and Marohn, J. A. Batch-fabrication of cantilevered magnets on attonewton-sensitivity mechanical oscillators for scanned-probe nanoscale magnetic resonance imaging. *ACS Nano*, 4(12):7141–7150, 2010.

[204] Garner, S. R. Force-gradient detection of nuclear magnetic resonance. PhD thesis, Cornell University, 2005.

[205] Donkersloot, R. Exploring a novel cantilever design for enhanced sensitivity in magnetic resonance force microscopy. Master's thesis, Cornell University, 2016.

[206] OConnell, A. D., Ansmann, M., Bialczak, R. C., Hofheinz, M., Katz, N., Lucero, E., McKenney, C., Neeley, M., Wang, H., Weig, E. M., Cleland, A. N., and Martinis, J. M. Microwave dielectric loss at single photon energies and millikelvin temperatures. *Appl. Phys. Lett.*, 92(11):112903, 2008.

[207] Gao, J., Daal, M., Vayonakis, A., Kumar, S., Zmuidzinas, J., Sadoulet, B., Mazin, B. A., Day, P. K., and Leduc, H. G. Experimental evidence for a surface distribution of two-level systems in superconducting lithographed microwave resonators. *Appl. Phys. Lett.*, 92(15):152505, 2008.

[208] Gao, J., Daal, M., Martinis, J. M., Vayonakis, A., Zmuidzinas, J., Sadoulet, B., Mazin, B. A., Day, P. K., and Leduc, H. G. A semiempirical model for

two-level system noise in superconducting microresonators. *Appl. Phys. Lett.*, 92(21):212504, 2008.

[209] Vissers, M. R., Kline, J. S., Gao, J., Wisbey, D. S., and Pappas, D. P. Reduced microwave loss in trenched superconducting coplanar waveguides. *Appl. Phys. Lett.*, 100(8):082602, 2012.

[210] Oliver, W. D. and Welander, P. B. Materials in superconducting quantum bits. *MRS Bull.*, 38(10):816825, 2013.

[211] Wendin, G. Quantum information processing with superconducting circuits: a review. *Rep. on Prog. Phys.*, 80(10):106001, 2017.

[212] Wang, J., Zhang, W., Zhang, J., You, J., Li, Y., Guo, G., Feng, F., Song, X., Lou, L., Zhu, W., and Wang, G. Coherence times of precise depth controlled NV centers in diamond. *Nanoscale*, 8(10):5780–5785, 2016.

[213] Brandenburg, F., Nagumo, R., Saichi, K., Tahara, K., Iwasaki, T., Hatano, M., Jelezko, F., Igarashi, R., and Yatsui, T. Improving the electron spin properties of nitrogen-vacancy centres in nanodiamonds by near-field etching. *Sci. Rep.*, 8 (1):15847, 2018.

[214] Martinis, J. M., Cooper, K. B., McDermott, R., Steffen, M., Ansmann, M., Osborn, K. D., Cicak, K., Oh, S., Pappas, D. P., Simmonds, R. W., and Yu, C. C. Decoherence in Josephson qubits from dielectric loss. *Phys. Rev. Lett.*, 95:210503, Nov 2005.

[215] Sendelbach, S., Hover, D., Kittel, A., Mück, M., Martinis, J. M., and McDermott, R. Magnetism in SQUIDs at millikelvin temperatures. *Phys. Rev. Lett.*, 100:227006, Jun 2008.

[216] Sendelbach, S., Hover, D., Mück, M., and McDermott, R. Complex inductance, excess noise, and surface magnetism in dc SQUIDs. *Phys. Rev. Lett.*, 103(11): 117001, 2009.

[217] Sank, D., Barends, R., Bialczak, R. C., Chen, Y., Kelly, J., Lenander, M., Lucero, E., Mariantoni, M., Megrant, A., Neeley, M., O'Malley, P. J. J., Vainsencher, A., Wang, H., Wenner, J., White, T. C., Yamamoto, T., Yin, Y., Cleland, A. N., and Martinis, J. M. Flux noise probed with real time qubit tomography in a josephson phase qubit. *Physycal Rev. Lett.*, 109:067001, Aug 2012.

[218] Wang, C., Axline, C., Gao, Y. Y., Brecht, T., Chu, Y., Frunzio, L., Devoret, M., and Schoelkopf, R. J. Surface participation and dielectric loss in superconducting qubits. *Appl. Phys. Lett.*, 107(16):162601, 2015.

[219] Chu, Y., Axline, C., Wang, C., Brecht, T., Gao, Y. Y., Frunzio, L., and Schoelkopf, R. J. Suspending superconducting qubits by silicon micromachining. *Appl. Phys. Lett.*, 109(11):112601, 2016.

[220] Quintana, C. M., Megrant, A., Chen, Z., Dunsworth, A., Chiaro, B., Barends,

R., Campbell, B., Chen, Y., Hoi, I.-C., Jeffrey, E., Kelly, J., Mutus, J. Y., O'Malley, P. J. J., Neill, C., Roushan, P., Sank, D., Vainsencher, A., Wenner, J., White, T. C., Cleland, A. N., and Martinis, J. M. Characterization and reduction of microfabrication-induced decoherence in superconducting quantum circuits. *Appl. Phys. Lett.*, 105(6):062601, 2014.

[221] Dial, O., McClure, D. T., Poletto, S., Keefe, G., Rothwell, M. B., Gambetta, J. M., Abraham, D. W., Chow, J. M., and Steffen, M. Bulk and surface loss in superconducting transmon qubits. *Supercond. Science Technol.*, 29(4):044001, 2016.

[222] Bosman, S. J. Delft Circuits b.v. URL `https://www.delft-circuits.com/`.

[223] Ong, F. R., Orgiazzi, J.-L., de Waard, A., Frossati, G., and Lupascu, A. Insertable system for fast turnaround time microwave experiments in a dilution refrigerator. *Rev. Sci. Instruments*, 83(9):093904, 2012.

[224] Wollersheim, O., Zumaqué, H., Hormes, J., Kadereit, D., Langen, J., Häußling, L., Hoessel, P., and Hoffmann, G. Quantitative studies of the radiation chemical behaviour of PMMA and poly(lactides). *Nucl. Instruments Methods Phys. Res. Section B: Beam Interactions with Mater. Atoms*, 97(1):273 – 278, 1995. ISSN 0168-583X.

[225] Rangan, S., Bartynski, R. A., Narasimhan, A., and Brainard, R. L. Electronic structure, excitation properties, and chemical transformations of extreme ultraviolet resist materials. *J. Appl. Phys.*, 122(2):025305, 2017.

[226] Thete, A., Geelen, D., van der Molen, S. J., and Tromp, R. M. Charge catastrophe and dielectric breakdown during exposure of organic thin films to low-energy electron radiation. *Phys. Rev. Lett.*, 119(26):266803, 2017.

[227] Valiev, K. A. The physics of submicron lithography. *Springer Science & Business Media*, 2012.

[228] Biercuk, M. J., Uys, H., Britton, J. W., VanDevender, A. P., and Bollinger, J. J. Ultrasensitive detection of force and displacement using trapped ions. *Nature Nanotechnol.*, 5(9):646–650, 2010.

[229] Poot, M. and van der Zant, H. S. J. Mechanical systems in the quantum regime. *Phys. Rep.*, 511(5):273–335, 2012.

[230] Moser, J., Güttinger, J., Eichler, A., Esplandiu, M. J., Liu, D. E., Dykman, M. I., and Bachtold, A. Ultrasensitive force detection with a nanotube mechanical resonator. *Nature Nanotechnol.*, 8(7):493–496, 2013.

[231] Norte, R. A., Moura, J. P., and Gröblacher, S. Mechanical resonators for quantum optomechanics experiments at room temperature. *Phys. Rev. Lett.*, 116 (14):147202, 2016.

[232] Rocheleau, T., Ndukum, T., Macklin, C., Hertzberg, J. B., Clerk, A. A., and Schwab, K. C. Preparation and detection of a mechanical resonator near the

ground state of motion. *Nature*, 463(7277):72–75, 2010.

[233] Tao, Y. and Degen, C. L. Single-crystal diamond nanowire tips for ultrasensitive force microscopy. *Nano Lett.*, 15(12):7893–7897, 2015.

[234] Garbini, J. L., Bruland, K. J., Dougherty, W. M., and Sidles, J. A. Optimal control of force microscope cantilevers. I. controller design. *J. Appl. Phys.*, 80 (4):1951–1958, 1996.

[235] Bruland, K. J., Garbini, J. L., Dougherty, W. M., and Sidles, J. A. Optimal control of force microscope cantilevers. ii. magnetic coupling implementation. *J. Appl. Phys.*, 80(4):1959–1964, 1996.

[236] Marshall, W., Simon, C., Penrose, R., and Bouwmeester, D. Towards quantum superpositions of a mirror. *Phys. Rev. Lett.*, 91(13):130401, 2003.

[237] Armour, A. D., Blencowe, M. P., and Schwab, K. C. Entanglement and decoherence of a micromechanical resonator via coupling to a cooper-pair box. *Phys. Rev. Lett.*, 88(14):148301, 2002.

[238] Van Wezel, J. and Oosterkamp, T. H. A nanoscale experiment measuring gravity's role in breaking the unitarity of quantum dynamics. In *Proceedings of the Royal Society A*, volume 468, pages 35–56. The Royal Society, 2012.

[239] Cohadon, P.-F., Heidmann, A., and Pinard, M. Cooling of a mirror by radiation pressure. *Phys. Rev. Lett.*, 83(16):3174, 1999.